UNIVERSITY OF OKLAHOMA

GRADUATE COLLEGE

IMPACT OF MICROPHYSICS PARAMETERIZATION SCHEMES ON THE ASSIMILATION OF GOES-16 ABI ALL-SKY INFRARED RADIANCES FOR A BOW ECHO ANALYSIS AND PREDICTION

A THESIS

SUBMITTED TO THE GRADUATE FACULTY

in partial fulfillment of the requirements for the

Degree of

MASTER OF SCIENCE

By

YU-SHIN KIM

Norman, Oklahoma

2023

IMPACT OF MICROPHYSICS PARAMETERIZATION SCHEMES ON THE ASSIMILATION OF GOES-16 ABI ALL-SKY INFRARED RADIANCES FOR A BOW ECHO ANALYSIS AND PREDICTION

A THESIS APPROVED FOR THE

SCHOOL OF METEOROLOGY

BY THE COMMITTEE CONSISTING OF

Dr. Xuguang Wang (Chair)

Dr. Aaron Johnson (Co-Chair)

Dr. Greg McFarquhar

Acknowledgements

I am deeply grateful to my advisors, Dr. Xuguang Wang and Dr. Aaron Johnson, for their exceptional guidance and unwavering support throughout the entire course of my research for this thesis. Their expertise and advice have been instrumental in shaping me as a scientist. Their willingness to provide guidance at every step of the journey has been invaluable, and I cannot thank them enough for the time and effort they invested in helping me succeed. I would also like to extend my heartfelt thanks to my committee member, Dr. Greg McFarquhar, for his additional support and valuable feedback, which played a significant role in further improving my thesis. I am immensely grateful to Dr. Nicholas Gasperoni and Dr. Yongming Wang for their invaluable assistance in the initial setup of my experiments. Furthermore, I would like to express my gratitude to all the members of the Multiscale data Assimilation and Predictability (MAP) laboratory. The discussions and encouragement I received from each one of you have been both inspiring and motivating. Lastly, I am honored to be a part of this exceptional team, and I genuinely treasure the time spent with all of you.

The work is primarily supported from the National Oceanic and Atmospheric Administration (NOAA) by the NA16OAR4320115 and NA21OAR4320204 grants. This work used the Stampede2 at the Texas Advanced Computing Center (TACC) through allocation ATM140042 from the Advanced Cyberinfrastructure Coordination Ecosystem: Services & Support (ACCESS) program, which is supported by National Science Foundation grants #2138259, #2138286, #2138307, #2137603, and #2138296. Computing for this project was also performed at the University of Oklahoma Supercomputing Center for Education and Research (OSCER).

Table of Contents

List of Tables

List of Figures

Abstract

Assimilating infrared brightness temperature (BT) from the water vapor sensitive channels of the GOES-16 Advanced Baseline Imager (ABI) has been shown by past studies to improve the analysis and prediction of severe weather events. These studies are limited to using a single microphysics scheme. Microphysics schemes are expected to affect bow echo dynamics and BT. Therefore, this study aims to investigate how assimilating GOES-16 ABI infrared BT with different microphysics schemes affects the analysis and prediction of the 3 May 2020 bow echo case. The Gridpoint Statistical Interpolation based Ensemble Kalman Filter (GSI-EnKF) system and Weather Research and Forecasting (WRF) model are utilized to conduct data assimilation (DA) experiments using Thompson, WDM6, NSSL, and Morrison microphysics schemes.

Correlation structures between BT and model state variables indicate that assimilating infrared BT can adjust bowing MCS dynamics via latent cooling and the rear inflow jet. Such corrections during DA cycling enhance the rear inflow jet and bow echo size, primarily for microphysics schemes featuring faster hydrometeor fall velocity and stronger latent cooling. The improved analyses lead to better forecasts of the bow echo's shape, size, timing of the bowing process, and wind speeds. Substituting a larger microphysics-dependent effective radius for a constant default value increases prior BT, the magnitude of BT innovations, and accumulated impact on the rear inflow jet, especially for the WDM6 and Morrison schemes. In the subsequent forecasts, incorporating microphysics-dependent effective radius further improves the experiment using the Morrison scheme but degrades it when using the WDM6 scheme.

Chapter 1

Introduction

The all-sky infrared radiances observed by the water vapor channels aboard geostationary satellites, such as the Advanced Baseline Imager (ABI) of the Geostationary Operational Environmental Satellite series (e.g., GOES-16), provide high spatial and temporal resolution data on humidity and clouds at storm scales. The data assimilation (DA) of such brightness temperature (BT) observations from the radiance data has improved the analysis and prediction of severe weather events, including extratropical cyclones (Otkin 2012; Jones et al. 2013; Jones et al. 2014), tropical cyclones (Zhang et al. 2016; Minamide and Zhang 2018; Honda et al. 2018a; Honda et al. 2018b; Chan et al. 2020), tornadic supercells (Kerr et al. 2015; Zhang et al. 2018; Jones et al. 2020; Chandramouli et al. 2022; Johnson et al. 2022; Zhang et al. 2022), and mesoscale convective systems (MCSs, Cintineo et al. 2016; Jones et al. 2020; Zhu et al. 2023).

The studies mentioned earlier have not specifically investigated the potential influence of microphysics schemes on the assimilation of all-sky infrared BT for severe weather events. Given the various ways that a microphysics scheme influences model hydrometeors and storm dynamics, such investigation may lead to more effective assimilation of all-sky infrared BT. For example, the depiction of latent cooling in the model's background state vector and background error covariance metric varies based on the chosen microphysics scheme (Adams-Selin et al. 2013b; Wheatley et al. 2014; Feng et al. 2018), which may impact the overall results of DA. The hydrometeor fall velocity, which varies depending on the chosen microphysics scheme, impacts the prior BT by modifying the vertical profiles of hydrometeors (Van Weverberg et al. 2013; Jones

et al. 2018; Feng et al. 2018; Griffin and Otkin 2022), along with the influence of model dynamics (Hamada and Takayabu 2016). The hydrometeor profile serves as one of the input parameters in a radiative transfer model. The particle size, which is specified differently depending on the chosen microphysics scheme, can affect the simulated prior BT as input to a radiative transfer model (Prabhakara et al. 1988; Fu and Liou 1993; McFarquhar and Heymsfield 1998; McFarquhar et al. 2003; Mitchell et al. 2008; Liu et al. 2014; Wang et al. 2020).

Previous studies (Cintineo et al. 2016; Jones et al. 2020; Zhu et al. 2023) have demonstrated that assimilating infrared BT improves cloud structures for MCS events, in particular. However, limited explanations have been provided regarding the impact of assimilating BT on MCS dynamics and subsequent MCS forecasts. One would expect that cloud structures, particularly trailing stratiform regions of a bowing MCS, play a critical role in the formation and development of the rear inflow jet due to vorticity augmentation and latent cooling. Firstly, vorticity augmentation occurs within stratiform clouds between the front-to-rear outflow aloft and the spreading cold pool near surface, which induces the rear inflow jet (Lafore and Moncrieff 1989; Weisman 1992). Secondly, latent cooling resulting from evaporation, sublimation, and melting of hydrometeors within stratiform clouds influences the structure and strength of the rear inflow jet through an enhanced horizontal buoyancy gradient between the leading convection and stratiform clouds (Fovell and Ogura 1988; Szeto and Cho 1994; Adams-Selin et al. 2013a).

This study assimilates GOES-16 ABI all-sky infrared BT to investigate how different microphysics parameterization schemes affect the analysis and prediction of a typical bow echo case. As part of diagnosing the influences of different microphysics schemes, more in-depth diagnostics are provided to assess the impact of assimilating all-sky infrared BT on simulating bow echo dynamics. Section 2 provides a case overview, model and data assimilation

configuration, how to improve the consistency in effective radius, experiment design, and verification methods. The results of the analysis and prediction of the bow echo are presented in Section 3, while Section 4 contains conclusions.

Chapter 2

Methodology

2.1 Case overview

A typical bow echo event that occurred on 3 May 2020 is selected for the analysis and prediction of a bowing MCS. This case was characterized by straight-line wind damage, including 267 wind reports and one EF-1 tornado, and resulted in one fatality and three injuries across Kansas, Missouri, Arkansas, Kentucky, Tennessee, and Alabama, according to the Storm Prediction Center (SPC). The bowing MCS began its convective initiation over Kansas at 0930 UTC and became an organized MCS by 1200 UTC as it moved southeastward (Fig. 1a). Its bowing process started at 1500 UTC as the upright structure of the MCS transitioned to an upshear-tilted structure, expanding a trailing stratiform region behind the leading convection (Figs. 1b,c). Between 1700 and 1900 UTC (Figs. 1d,e), radar reflectivity revealed prominent bow shapes as the rear inflow jet developed within the trailing stratiform clouds. This led to sharp increases in wind reports along the swath of the bow echo, as the rear inflow jet reached down to the surface. The radar reflectivity greater than 50 dBZ and rear inflow notch pattern appeared at the northern part of the leading convection, likely due to the presence of the mesoscale convective vortex (MCV, Fig. 1e), as explained by previous studies (Trapp and Weisman 2003; Atkins et al. 2004; Wheatley et al. 2006; Atkins and Laurent 2009). Between 1900 and 2100 UTC (Figs. 1e,f), the bowing MCS reached its mature stage in size and the number of wind reports before dissipating at 0000 UTC (Fig. 1g). The entire life cycle of the bow echo is consistent with the previous study by Fujita (1978) on the typical evolution of a bow echo.

2.2 Model and data assimilation configuration

To simulate the bowing MCS, this study utilizes version 4.3.1 of the Weather Research and Forecasting (WRF) Advanced Research WRF (ARW) model (Skamarock et al., 2019) model, due to its capability of representing mesoscale and convective phenomena. The configuration used in the current study, as summarized in Table 1, is based on previous studies that analyzed and predicted convective-scale phenomena, such as Gasperoni et al. (2020) and Johnson et al. (2022). The model domain covers the central and eastern continental United States (Fig. 2), with a 3 km grid spacing and 51 vertical layers up to 50 hPa, to resolve convective-scale features adequately. The model physics configuration includes the Rapid Radiative Transfer Model for GCMs scheme (RRTMG, Mlawer et al. 1997) for both long-wave and short-wave, the Mellor-Yamada-Nakashi-Niino scheme (MYNN, Nakanishi and Niino 2009) for the planetary boundary layer, the Noah land surface model (Niu et al. 2011), and no cumulus parameterization. The microphysics parameterization schemes used in this study are introduced later in Section 2.4.

The Gridpoint Statistical Interpolation based Ensemble Kalman Filter (GSI-EnKF, Whitaker et al. 2008; Wang et al. 2013; Wang and Lei 2014) is employed to assimilate GOES-16 ABI infrared BT, ground-based radar reflectivity, and conventional observations. The GSI-EnKF system is capable of directly assimilating radar reflectivity with state vectors of vertical velocity and hydrometeor mixing ratios, including ice, snow, graupel, cloud, and rain species (Johnson et al. 2015; Wang and Wang 2017). The GSI-EnKF system has the ability to assimilate ABI all-sky BT and update hydrometeor mixing ratios using version 2.3 of the CRTM (Han et al. 2006), following the same configuration as described in Johnson et al. (2022).

The initial ensemble members are initialized by selecting 20 members from the 0600 UTC 3 May analyses and 20 members from the 0000 UTC 3 May forecasts of the NCEP Global

Ensemble Forecast System (GEFS, Zhou et al. 2017), resulting in a total of 40 ensemble members. Conventional data, such as surface and upper-level observations, are assimilated hourly from 0700 UTC to 1500 UTC during the spin up of convective scale features (Fig. 3). As the MCS of interest develops, Multi-Radar Multi-Sensor (MRMS, Zhang et al. 2016) radar reflectivity mosaics are assimilated on an hourly basis between 1000 UTC and 1300 UTC. Subsequently, radar reflectivity is assimilated every 10 minutes to enhance the structure of the organized MCS between 1310 UTC and 1500 UTC. As part of the experiments, the assimilation of GOES-16 ABI observations includes channel 10 all-sky infrared BT data at a wavelength of 7.3 μm during prominent bowing processes between 1510 UTC and 1800 UTC.

The GOES-16 ABI level 1 radiance observation data are converted into BTs and thinned from their original 2 km resolution to a 6 km resolution, covering the region of interest along the path of the MCS propagation during the assimilation period, as highlighted by the red box in Fig. 2. Outside the region of interest, the BTs are thinned to a 12 km resolution. In a preliminary experiment, regions with observed high clouds but insufficient high clouds in the background ensemble resulted in excessively large water vapor increments, leading to spurious convection. This is avoided in the present study by excluding pixels with high clouds above 300 hPa only in the observation but not in the ensemble mean background.

During the DA cycling, the posterior covariance is inflated using the Relaxation to Prior Spread (RTPS) method (Whitaker and Hamill 2012) with a factor of 0.80 to preserve ensemble spread. Localization and observation error parameters are configured separately for each observation dataset. For covariance localization of the conventional observations, the DA system is configured with a horizontal localization cut-off of 300 km and a vertical localization cut-off of 1.1 units in natural logarithmic pressure, using Gaspari and Cohn's (1999) localization function.

The observation errors employed for the conventional observations are consistent with those utilized in the Rapid Refresh (RAP, Benjamin et al. 2016). The horizontal and vertical localizations of radar reflectivity utilize cut-off distances of 15 km and 1.1 units in natural logarithmic pressure, respectively, following Johnson et al. (2015) and Wang and Wang (2017). A radar reflectivity observation error of 5 dBZ is employed, following Dowell and Wicker (2009), Aksoy et al. (2009), and Yussouf et al. (2013). A horizontal localization cut-off of 15 km is adopted for ABI infrared BT observations, following Johnson et al. (2022). The DA system employs a vertical localization cut-off of 3.3 units for BT in natural logarithmic pressure, with similar values to those used in Jones et al. (2018) and Zhu et al. (2023). For BT localization, the heights of ABI BT observations are determined based on the estimated heights of the maximum weighting function. A BT observation error of 3 K is used, based on Minamide and Zhang (2017), Zhang et al. (2018), and Zhu et al. (2023).

2.3 Consistency in effective radius between forward operator and microphysics scheme

The GSI system currently utilizes constant default values for the hydrometeor effective radius, which represents the mean scattered particle size, regardless of the selected microphysics scheme, when simulating prior BT. The assigned effective radius values are as follows: ice (30 μm), snow (600 μm), graupel (600 μm), cloud (10 μm), and rain (300 μm). The utilization of a constant default effective radius in the GSI system results in an inconsistency in particle size between the microphysics schemes and the radiative transfer model employed for the BT observation operator.

One approach to improve consistency in simulating prior BT is to utilize the effective radius calculated based on the microphysics scheme, instead of using a constant default value. This approach has been employed in previous studies on microphysics-radiation interactions in numerical weather prediction models (Baran et al. 2014; Thompson et al. 2016; Bae et al. 2016; Bae et al. 2019). However, this approach for infrared radiance is limited compared to previous studies that improved the consistency for microwave channels by employing identical particle size distributions (Sieron et al. 2017), mass-size relationships (Ren et al. 2023), and particle shapes (Sieron et al. 2018; Moradi et al. 2022). The use of effective radius in CRTM computed as in the microphysics scheme is referred to as a microphysics-dependent effective radius (MP dep. $\boldsymbol{r_e}$).

The microphysics-dependent effective radius can be calculated based on a given particle size distribution $N(r)$, which is assumed within each microphysics scheme. The effective radius (r_e) is defined using the third moment divided by the second moment of the particle size distribution (Parol et al. 1991; McFarquhar and Heymsfield 1996), which is expressed as,

$$r_e = \frac{\int r^3 N(r) dr}{\int r^2 N(r) dr} \tag{1}$$

where r is hydrometeor radius. This study utilizes the microphysics-dependent effective radius, which is calculated within the microphysics subroutines in WRF version 4.3.1 (Thompson et al. 2016; Bae et al. 2016).

The impact of microphysics-dependent effective radius on simulating prior BT can be understood by considering the relationship between the effective radius of hydrometeors and their optical thickness. This relationship, as shown in Stephens (1978), can be approximated for a spherical shape as follows,

$$\tau \approx \frac{3Q_e L}{4\rho_h r_e} \tag{2}$$

where τ represents the optical thickness, Q_e is the extinction efficiency, L denotes the liquid or ice water path, q_h and r_e represent the hydrometeor density and effective radius, respectively. As the optical thickness decreases, transmittance exhibits an exponential increase, making the ABI sensor at the top of the atmosphere more sensitive to radiance emitted from particles at lower heights with higher temperatures in the troposphere. Firstly, increasing the effective radius results in a decrease in optical thickness. Consequently, replacing the default constant value with a larger microphysics-dependent effective radius increases prior BT. Secondly, optical thickness is directly proportional to the ice or liquid water path, which is in turn proportional to the hydrometeor mixing ratio. Hence, if the hydrometeor mixing ratio and corresponding optical thickness are high enough to attenuate radiances mostly, the impact of changes in effective radius on prior BT will be insignificant. Thirdly, optical thickness is inversely proportional to hydrometeor density. As a result, optical thickness and prior BT are more sensitive to the changes in effective radius of ice or cloud particles, which have a higher density compared to snow particles.

2.4 Experiment design

Four microphysics parameterization schemes have been selected for this study: Thompson (Thompson et al. 2008), National Severe Storms Laboratory 2-moment scheme (NSSL, Mansell et al. 2010), WRF Double Moment 6-class scheme (WDM6, Lim and Hong 2010), and Morrison 2-moment scheme (Morrison et al. 2009). The chosen microphysics schemes, classified as partial

or full 2-moment schemes, are preferred for their ability to accurately represent latent cooling in stratiform clouds compared to 1-moment schemes (Morrison et al. 2008; Wheatley et al. 2014).

Table 2 provides a summary of differences in latent cooling and prior BT in the four microphysics schemes. Regarding BT characteristics, the Thompson scheme produces the most realistic BT for prior characteristics compared to satellite observations, primarily due to the slow fall velocity of snowflakes near the cloud top (Van Weverberg et al. 2013; Jones et al. 2018; Feng et al. 2018). In contrast, the NSSL scheme generates lower BT compared to the Thompson scheme, primarily attributed to relatively slower ice and snow fall velocities (Jones et al. 2018; Griffin and Otkin 2022). However, these velocities are adjusted to achieve comparable BT to the Thompson scheme and observations (Jones et al. 2018). Due to its faster ice fall velocity (Van Weverberg et al. 2013) and the use of identical parameterizations for solid hydrometeor species as the WRF Single Moment 6-class scheme (WSM6, Hong and Lim 2006), the WDM6 scheme is expected to generate higher BT compared to the Thompson scheme. The Morrison scheme produces lower BT compared to the Thompson scheme due to the slower ice fall velocity (Van Weverberg et al. 2013; Feng et al. 2018).

Regarding latent cooling, the Thompson scheme has been found to generate strong cooling near the surface (Feng et al. 2018), while the NSSL scheme produces weaker cooling than the Thompson scheme (Wheatley et al. 2014). Conversely, the WDM6 scheme generates even stronger latent cooling compared to the Thompson scheme (Adams-Selin et al. 2013b), while the Morrison scheme produces weaker latent cooling than the Thompson scheme (Feng et al. 2018).

The DA experiments are designed to investigate the impacts of assimilating only infrared BT during the bowing process of the MCS. Table 3 provides a summary of the overall experiment design. In this study, baseline experiments are conducted for each microphysics scheme,

assimilating conventional observations and radar reflectivity while excluding BT assimilation (Fig. 3). Starting at 1200 UTC, separate baseline experiments using different microphysics schemes are performed, initialized from the same 1200 UTC ensemble analyses utilizing the Thompson scheme. In each baseline experiment, a 9-hour deterministic forecast is initiated at 1500 UTC, utilizing the ensemble mean analysis specific to the corresponding experiment. The first objective of the baseline experiments is to evaluate the simulated bowing MCS in experiments with and without BT assimilation within each microphysics scheme. Additionally, the baseline experiment aims to compare the simulated bowing MCS among the baseline experiments using various microphysics schemes.

For each baseline experiment, a corresponding experiment is conducted by assimilating ABI infrared BT, using a constant default effective radius defined for each hydrometeor type in the current GSI system. These experiments, referred to as the ABI constant effective radius experiments (ABI const. $\boldsymbol{r_e}$), are conducted through 10-minute BT assimilation cycles from 1510 UTC to 1800 UTC, followed by deterministic forecasts from 1800 UTC to 0000 UTC. The purpose of these experiments is to explore how different fall velocity assumptions and latent cooling inherent in microphysics schemes affect the analysis increments associated with the dynamics of the bowing MCS. In these experiments, the impact of latent cooling is examined by comparing the Thompson and NSSL schemes, while the impact of hydrometeor fall velocity is explored by comparing the Thompson and NSSL schemes with the WDM6 and Morrison schemes. Section 3.2 elaborates on the results of the analysis, followed by deterministic forecasts discussed in Sections 3.4 and 3.5.

An additional set of experiments, called the ABI microphysics-dependent effective radius experiments (ABI MP dep. $\boldsymbol{r_e}$), is conducted. These experiments follow the same design as the

ABI constant effective radius experiments, but with microphysics-dependent effective radius calculated based on each microphysics scheme. The experiments aim to investigate how variations in effective radius across microphysics schemes could impact the prior BT, BT innovations, and analysis increments related to the dynamics of the bowing MCS. Section 3.3 evaluates the impact of microphysics-dependent effective radius during DA cycling by comparing it with the ABI constant effective radius experiments. The results of deterministic forecasts are also presented in Sections 3.4 and 3.5.

To validate the deterministic forecasts, the reflectivity forecasts are compared to MRMS radar reflectivity using the fractions skill score (FSS, Roberts and Lean 2008) with a 36 km radius of influence. Specifically, the forecasted bow shape and size in the leading convection are evaluated using a reflectivity threshold of 35 dBZ, which indicates convective precipitation (Zipser and Lutz 1994). To further demonstrate the improvement achieved by assimilating BT over their respective baseline experiments, the relative improvement in FSS (Schiemann et al. 2018) is also calculated.

Chapter 3

Results

3.1 Correlation structures of brightness temperature in bowing MCS

In an Ensemble Kalman Filter (EnKF), correlation structures between BTs and model state variables have been used to reveal the impact of assimilating BT on model state variables for an extratropical cyclone (Jones et al. 2014), tornadic supercells (Kerr et al. 2015; Zhang et al. 2022), and an MCS case (Zhu et al. 2023). Here, the correlation structures between BTs and model state variables are used to evaluate how assimilating infrared BT specifically corrects the dynamics of a bowing MCS using the Thompson microphysics scheme. The correlation structures of the BT at the leading convection and trailing stratiform regions are calculated from the 1700 UTC ensemble analyses during periods of prominent bowing process at the leading convection and trailing stratiform regions, separately.

The leading convection exhibits upshear-tilted convective scale updrafts, resulting in ascending front-to-rear outflow aloft along the trailing stratiform region (Fig. 4a). The trailing stratiform region shows low relative humidity and equivalent potential temperature below the height of 5 km, indicating latent cooling and a cold pool. The latent cooling induces negative buoyancy, leading to the descent of the rear inflow jet towards the leading convection.

In the leading convection (Fig. 4b), the BTs negatively correlate with water vapor mixing ratios and potential temperature in the middle and upper troposphere, exhibiting an upshear-tilted structure. These correlation structures indicate moistening and intensifying latent heating when observed BT is lower than prior BT. Over the same region, the positive correlation of horizontal

winds and negative correlations of vertical winds with BTs suggest a corresponding enhancement of front-to-rear outflow and updrafts.

In the trailing stratiform region (Fig. 4c), the BTs negatively correlate with water vapor mixing ratios and potential temperature in the upper troposphere and positively correlate with potential temperature in the lower troposphere. These correlation patterns suggest moistening and intensifying latent heating aloft but latent cooling below. Collocated with the moistening and latent heating aloft, the positive correlations of horizontal winds and negative correlations of vertical winds with BTs in the upper troposphere indicate a corresponding enhancement of ascending front-to-rear outflow. Collocated with the latent cooling below, the positive correlations of vertical winds with the BTs in the lower troposphere indicate a resultant downdraft. Over the same region, the horizontal winds correlate negatively with BTs at 4-5 km heights but positively below 3 km height, suggesting a corresponding reinforcement of the rear inflow jet and cold pool motion, respectively.

The above BT correlation structures are consistent with bowing MCS dynamics in previous studies on the role of vorticity augmentation, which induces rear inflow jet between front-to-rear outflow at mid-levels and cold pool motion at low-levels (Lafore and Moncreiff 1989; Weisman 1992). Specifically, the correlation structures also correspond to the roles of latent cooling in the stratiform region, promoting a cold pool (Lin et al. 1983; Lafore and Moncrieff 1989; Weisman and Rotunno 2005), descending rear inflow jet (Weisman 1992; Pandya and Durran 1996; Pandya et al. 2000; Grim et al. 2009b), and enhancing the speed of the rear inflow jet (Chen and Cotton 1988; Szeto and Cho 1994). In summary, the assimilation of infrared BT can correct bowing MCS dynamics by updating front-to-rear outflow, latent cooling, and the rear inflow jet, even though the infrared BT are mostly sensitive to hydrometeors near the cloud top.

3.2 Impact of microphysics schemes during DA cycling

The differences in BT innovations and corresponding accumulated impacts on bowing MCS dynamics are examined during DA cycling to understand the impact of microphysics schemes on the ABI BT assimilation. During the DA cycling from 1510 to 1800 UTC (Figs. 5a,b), the MCS evolved into a bow echo through prominent bowing processes developing within its expanding trailing stratiform clouds, observed through low BT by GOES-16 ABI.

All experiments using the four microphysics schemes show limited coverage of trailing stratiform clouds within the MCS in the ensemble mean of the first-guess at the first (1510 UTC) ABI cycle (Fig. 5c). Moreover, the simulated prior BTs are higher compared to the observed values. Spurious clouds are generated southeast of the MCS in the first-guess.

Although all experiments demonstrate higher prior BTs over the trailing stratiform region in the first-guess, the experiment using microphysics schemes with fast fall velocity produces much higher prior BTs than observed, leading to more negative BT innovations (Fig. 5d). The WDM6 scheme, assuming the fastest ice fall velocity, generates the highest prior BTs and the largest BT innovations, while the Morrison scheme, assuming the slowest ice fall velocity, produces the lowest prior BTs and the smallest BT innovations. The Thompson and NSSL schemes simulate similar prior BTs and BT innovations likely due to their comparable fall velocity assumptions.

These magnitudes of BT innovations lead to corresponding degrees of accumulated impact on the front-to-rear outflow at 200 hPa (Fig. 5e) and the rear inflow jet at 850 hPa (Fig. 5f) in each experiment. The accumulated impact on analysis during DA cycling is represented by differences between the ABI const. $\boldsymbol{r_e}$ and their respective Baseline experiments at the final ABI cycle. The

impact on the front-to-rear outflow and rear inflow jet are greatest in the WDM6 ABI const. $\boldsymbol{r_e}$ experiment and smallest in the Morrison ABI const. $\boldsymbol{r_e}$ experiment, reflecting their respective magnitudes of BT innovations. While the Thompson ABI const. $\boldsymbol{r_e}$ and NSSL const. $\boldsymbol{r_e}$ experiments exhibit similar impact on the front-to-rear outflow, the Thompson ABI const. $\boldsymbol{r_e}$ experiment shows greater impact on the rear inflow jet compared to the NSSL ABI const. $\boldsymbol{r_e}$ experiment. The experiments with a large magnitude of impact on the rear inflow jet exhibit a wide bow echo in the analyzed reflectivity at the final ABI cycle. As a result, the sizes of the analyzed bow echo follow the order of WDM6, Thompson, NSSL, and Morrison ABI const. $\boldsymbol{r_e}$ experiments.

The accumulated impacts on analysis are also calculated on cross-sections to assess the impacts of assimilating BT on the improved dynamics of the bowing MCS and understand the differences in the impact on the rear inflow jet between the Thompson and NSSL experiments. (Figs. 6,7). The increases in relative humidity in all ABI const. $\boldsymbol{r_e}$ experiments contribute to the expansion of the trailing stratiform clouds of the MCS (Fig. 6a). The enhanced front-to-rear outflow induces the rear inflow jet through vorticity augmentation (Fig. 6b), as proposed in the studies by Lafore and Moncreiff (1989) and Weisman (1992). The Thompson ABI const. $\boldsymbol{r_e}$ experiment exhibits more substantial negative impact on potential temperature below 4 km due to stronger latent cooling inherent in the Thompson scheme compared to the NSSL ABI const. $\boldsymbol{r_e}$ experiment. Hence, the more notable impact on the rear inflow jet shown in the Thompson ABI const. $\boldsymbol{r_e}$ experiment can be attributed to the corresponding impact on potential temperatures, aligning with the impact of the latent cooling on the rear inflow jet (Fovell and Ogura 1988; Szeto and Cho 1994; Adams-Selin et al. 2013a).

In summary, BT assimilation primarily corrects the trailing stratiform region due to the greater sensitivity of ABI BT observations to smaller hydrometeor particles, which radar may not detect. The experiments using microphysics schemes with fast fall velocity assumptions and strong latent cooling show large impact on the rear inflow jet and a wide bow echo in the analyzed reflectivity when assimilating ABI BT.

3.3 Impact of microphysics-dependent effective radius during DA cycling

The impact of microphysics-dependent effective radius on assimilating infrared BT for the bow echo event is investigated during ABI DA cycling by substituting the constant default effective radius. For the same first-guess at 1510 UTC, the differences in prior BT between the ABI MP dep. $\boldsymbol{r_e}$ and ABI const. $\boldsymbol{r_e}$ experiments are less than 1 K over the leading convection of the MCS for all microphysics schemes (Fig. 7a). Over the trailing stratiform region, both the Thompson and NSSL experiments demonstrate small differences of less than 1 K in prior BTs, similar to their respective leading convection. However, in the Morrison and WDM6 experiments, there are large differences greater than 1 K in prior BTs over the trailing stratiform region. The increases in prior BTs of the WDM6 ABI MP dep. $\boldsymbol{r_e}$ and Morrison ABI MP dep. $\boldsymbol{r_e}$ experiments result in more significant BT innovations and subsequent accumulated impacts at the final ABI cycle in the rear inflow jet (Fig. 7b), relative humidity (Fig. 7c), and potential temperature (Fig. 7d) compared to the respective ABI const. $\boldsymbol{r_e}$ experiment. The larger magnitudes of BT innovations in the Morrison ABI MP dep. $\boldsymbol{r_e}$ than the WDM6 ABI MP dep. $\boldsymbol{r_e}$ leads to greater degrees of impacts on the rear inflow jet, relative humidity, and potential temperature.

To illustrate the differences in prior BTs, vertical profiles of microphysical and optical properties are extracted from the first-guess at the leading convection and trailing stratiform clouds of the MCS. Over the leading convection, all experiments with the four microphysics schemes show a significant amount of hydrometeor mixing ratio, mainly due to optically thick snow particles (Fig. 8). The high optical thicknesses attenuate most radiances for both microphysics-dependent effective radius and constant default value, resulting in small differences in transmittance and subsequent BT weighting function. Therefore, the utilization of microphysics-dependent effective radius does not significantly impact the simulation of prior BTs over the leading convection of the MCS, regardless of the chosen microphysics schemes.

Over the trailing stratiform clouds, the Thompson and NSSL experiments exhibit high mixing ratios of optically thick snow, resulting in significant optical thickness regardless of the employed effective radius. (Figs. 9a,b). Hence, the BT weighting function and prior BTs are not sensitive to the variations in the effective radius for any hydrometeor type in this experiment. However, the WDM6 and Morrison experiments predominantly generate mixing ratios of optically thin ice instead of optically thick snow over the trailing stratiform clouds, leading to lower optical thicknesses compared to the respective leading convection. (Figs. 9c,d). Under low optical thickness conditions, using a microphysics-dependent effective radius larger than the constant default value for ice reduces the total optical thickness, leading to higher transmittance and lower heights of the BT weighting function. The decreased heights of the BT weighting function over the trailing stratiform clouds result in a higher prior BT for the WDM6 and Morrison experiments. In the Morrison experiments, the greater increase in the microphysics-dependent effective radius for ice leads to larger increases in prior BT compared to the WDM6 experiment.

In summary, the utilization of the microphysics-dependent effective radius has a significant impact primarily in the trailing stratiform region of the WDM6 and Morrison experiments. When optically thin ice is prevalent, using a microphysics-dependent effective radius larger than the constant default value for ice leads to higher prior BT and subsequent accumulated impact on the rear inflow jet during BT assimilation.

3.4 Reflectivity forecast and verification

The differences in 2 km AGL reflectivity forecasts of the bowing MCS size and shape are compared to the MRMS observations to understand the impact of microphysics schemes on the assimilation of ABI BT (Fig. 10a). The simulated bow echo in the Thompson Baseline experiment is smaller and persists for a shorter period compared to the observations (Fig. 10b). The Thompson ABI const. $\boldsymbol{r_e}$ experiment generates a wider bow echo compared to the Thompson Baseline and also forecasts a rear inflow notch pattern on the northern leading convection between 2000 and 2100 UTC. The Thompson ABI MP dep. $\boldsymbol{r_e}$ experiment exhibits qualitatively comparable reflectivity forecasts to the Thompson ABI const. $\boldsymbol{r_e}$, as the substitution of the constant default effective radius does not significantly affect the simulation of the prior BT in this case.

The NSSL Baseline experiment exhibits a smaller bow echo size and a delayed bowing process from 2000 to 2100 UTC, compared to the observed and Thompson Baseline, in accordance with the NSSL scheme's weaker latent cooling when compared to the Thompson scheme (Fig. 10c). The NSSL ABI const. $\boldsymbol{r_e}$ experiment generates an enlarged bow echo size, accompanied by an earlier bowing process at 1900 UTC, in contrast to the NSSL Baseline. The NSSL ABI MP dep. $\boldsymbol{r_e}$ experiment shows qualitatively comparable reflectivity forecasts to the NSSL ABI const. $\boldsymbol{r_e}$, as

the utilization of the microphysics-dependent effective radius does not have a significant impact on simulating the prior BT for the NSSL scheme.

The WDM6 Baseline experiment exhibits an earlier bowing process compared to other microphysics schemes, but the simulated bow echo moves faster than observed, in agreement with the significant latent cooling inherent in the WDM6 scheme (Fig. 11a). The WDM6 ABI const. $\boldsymbol{r_e}$ experiment demonstrates an enhanced bow shape and size compared to the WDM6 Baseline, but the simulated bow echo dissipates earlier than the observed after 2100 UTC. The WDM6 ABI MP dep. $\boldsymbol{r_e}$ experiment exhibits a slightly earlier dissipation of the bow echo over the southern leading convection compared to the WDM6 ABI const. $\boldsymbol{r_e}$.

The Morrison Baseline experiment produces the smallest bow echo among all the baselines, consistent with the weak latent cooling in the scheme (Fig. 11b). The Morrison ABI const. $\boldsymbol{r_e}$ experiment enhances the size of the bow echo compared to the Morrison Baseline. The Morrison ABI MP dep. $\boldsymbol{r_e}$ experiment exhibits an earlier bow echo at 2000 UTC compared to the Morrison ABI const. $\boldsymbol{r_e}$, and the experiment also forecasts the observed rear inflow notch pattern on the northern leading convection.

The above subjective evaluation of reflectivity forecasts is consistent with the objective verification of differences in baseline forecasts using FSS (Fig. 12a). Among all the Baseline experiments, WDM6 Baseline outperforms other Baseline experiments until 1900 UTC. However, after 2000 UTC, the FSSs of the WDM6 Baseline decline. These FSSs of the WDM6 Baseline correspond to the subjectively bow shape and size until 1900 UTC but too fast propagation of the MCS after 2000 UTC. Until 1900 UTC, the Morrison Baseline demonstrates the lowest performance, attributable to the smallest bow echo size between 1800 and 2000 UTC. The

Thompson Baseline outperforms the NSSL Baseline, corresponding to the earlier bowing process in the Thompson Baseline.

The impacts on skill resulting from assimilating ABI BT with constant or MP dep. $\boldsymbol{r_e}$ experiments are more clearly demonstrated through the relative improvements in FSS over their corresponding baselines (Fig. 12b,c). In almost every forecast hour, both the ABI const. $\boldsymbol{r_e}$ and ABI MP dep. $\boldsymbol{r_e}$ experiments consistently outperform their corresponding baseline experiments, consistent with the enhanced bow echo size achieved through the assimilation of ABI infrared BT. Among all ABI const. $\boldsymbol{r_e}$ experiments, the Morrison ABI const. $\boldsymbol{r_e}$ shows the most substantial improvement in FSS over the respective baseline until 1900 UTC, in accordance with the improve bow echo size. The NSSL ABI const. $\boldsymbol{r_e}$ experiment also demonstrates substantial improvement in FSS until 1900 UTC, in agreement with the improved timing of the bowing process. The WDM6 ABI const. $\boldsymbol{r_e}$ experiment demonstrates improved FSS over the WDM6 Baseline and exhibits the highest FSS at 1900 UTC (Fig. 12a), aligning with its notable bow shape and the widest bow echo size observed at 1900 UTC. After 2100 UTC, the WDM6 ABI const. $\boldsymbol{r_e}$ experiments experience a significant decrease in the relative improvement in FSSs, consistent with the earlier dissipation of the bow echo. The Thompson ABI MP dep. $\boldsymbol{r_e}$ experiment surpasses the Thompson Baseline and achieves the highest FSS at 2100 among all ABI const. $\boldsymbol{r_e}$ experiments, in accordance with its accurate forecasts of the rear inflow notch pattern.

The WDM6 ABI MP dep. $\boldsymbol{r_e}$ experiment exhibits poorer performance compared to the WDM6 ABI const. $\boldsymbol{r_e}$ experiment, in agreement with to the slight earlier dissipation of the bow echo. The Morrison ABI MP dep. $\boldsymbol{r_e}$ experiment shows additional improvement in FSS compared to the Morrison ABI const. $\boldsymbol{r_e}$ experiment, resulting in the highest FSS at 2000 UTC among all experiments, consistent with the refinement in the timing of the bowing process.

3.5 Surface wind forecast and verification

The impact of assimilating ABI BT on the reflectivity structures of the simulated bow echo, as depicted above, corresponds to differences in the prediction of severe surface wind. The simulated maximum wind speeds are validated against SPC wind reports between 1800 and 0000 UTC. The severe wind speeds exceeding 25 m s^{-1} were reported by SPC along the propagation of the bowing MCS (Fig. 13a). The most intense severe winds were observed in the northern swath, likely influenced by the MCV.

All baseline experiments employing four microphysics schemes generate a narrower swath of severe winds compared to the SPC reports, primarily due to the smaller size of the simulated bowing MCS (Fig. 13b). However, all ABI const. $\boldsymbol{r_e}$ experiments exhibit an enlarged area of severe winds due to the wider simulated bow echo, compared to their respective baseline experiments.

The ABI const. $\boldsymbol{r_e}$ experiments with a large bow echo size display a wide area of severe winds throughout the forecast. Hence, the order of severe wind areas corresponds to the WDM6, Thompson, NSSL, and Morrison ABI const. $\boldsymbol{r_e}$ experiments. Moreover, the Thompson ABI const. $\boldsymbol{r_e}$ exhibits wind speed peaks over the northern swath of severe winds, potentially related to the influence of the MCV.

Replacing the constant default effective radius leads to additional changes in wind swaths for the ABI MP dep. $\boldsymbol{r_e}$ experiments using the WDM6 and Morrison schemes. Compared to the WDM6 ABI const. $\boldsymbol{r_e}$, the WDM6 ABI MP dep. $\boldsymbol{r_e}$ exhibits a wider area of severe winds from 1800 to 2100 UTC due to the larger bow echo size, but narrower swaths from 2200 to 0000 UTC due to the earlier dissipation of the MCS. The Morrison ABI MP dep. $\boldsymbol{r_e}$ shows a wider swath of

severe winds from 1800 to 2000 UTC due to its earlier bowing process compared to the Morrison ABI const. $\boldsymbol{r_e}$. The Morrison ABI MP dep. $\boldsymbol{r_e}$ further predicts wind speed peaks over the northern swath associated with the MCV.

3.6 Evaluation of forecast rear inflow jet structure

The rear inflow jet plays a crucial role in the evolution of the bowing MCS and the generation of severe surface winds (Fujita 1978; Smull and Houze 1985 and 1987; Przybylinski 1995). Here, to understand the forecast differences in the rear inflow jet when assimilating ABI BT, the simulated storm-relative radial velocity is compared to WSR 88-D observations, following the studies by Atkins et al. (2004), Grim et al. (2009a), and Xu et al. (2015). The storm-relative radial velocity is obtained by subtracting the estimated storm motion, derived from MCS propagation in the MRMS reflectivity data, from the simulated radial velocity. The radial velocity is simulated based on the three-dimensional winds and hydrometeor fall velocity in the forecast.

The reflectivity field shows the observed bow echo characterized by the rear inflow notch pattern (Fig. 14a). The negative storm-relative radial velocity observed in the trailing stratiform region indicates the area and strength of the rear inflow jet (Fig. 14b). Additionally, the sharp storm-relative radial velocity gradient, aligned with the rear inflow notch pattern, indicates a cyclonic rotation associated with the MCV. The baseline experiments employing four microphysics schemes show smaller rear inflow jet areas compared to the observed values, resulting in narrower bow echo sizes and swaths of severe winds (Fig. 14c).

As ABI BT is assimilated, the ABI const. $\boldsymbol{r_e}$ experiments simulate an enlarged area of the rear inflow jet, resulting in wider bow echoes and larger areas of severe winds compared to their

respective baselines. The widest rear inflow jet in the WDM6 ABI const. $\boldsymbol{r_e}$ results in the widest bow echo size and the corresponding swath of severe winds. The smallest rear inflow jet in the Morrison ABI const. $\boldsymbol{r_e}$ leads to the smallest bow echo size and the corresponding swath of severe winds.

By incorporating microphysics-dependent effective radius, the WDM6 ABI MP dep. $\boldsymbol{r_e}$ and Morrison ABI MP dep. $\boldsymbol{r_e}$ experiments enhance the intensity of the rear inflow jet. The Morrison ABI MP dep. $\boldsymbol{r_e}$ experiment further increases the rotations of the MCV, resulting in improved maximum wind speeds.

Vertical cross-sections taken at 2000 and 2100 UTC further demonstrate the distinct effect of intensified rear inflow jets on the bowing MCS forecast in the WDM6 and Morrison ABI experiments (Fig. 15). The rear inflow jet in the WDM6 ABI const. $\boldsymbol{r_e}$ experiment does not exceed the leading convection at 2000 UTC, leading to the continuous initiation of new convective cells at 2100 UTC (Fig. 14a). The stronger rear inflow jet in the WDM6 ABI MP dep. $\boldsymbol{r_e}$ experiment compared to the WDM6 ABI const. $\boldsymbol{r_e}$ surpasses the leading convection at 2000 UTC, preventing the formation of new convection at 2100 UTC (Fig. 15b). Hence, the premature dissipation of the leading convection in the WDM6 ABI MP dep. $\boldsymbol{r_e}$ experiment can be attributed to the overestimated intensity of the rear inflow jet and cold pool. This overestimation is likely disrupting the balance between the low-level shear in the environment and the baroclinic shear at the edge of the cold pool, preventing maintenance of the MCS (Rotunno et al. 1988).

The Morrison ABI const. $\boldsymbol{r_e}$ experiment exhibits a weak rear inflow jet in the middle level at 2000 UTC, possibly due to inadequate impact on potential temperature related to latent cooling (Fig. 15c). At 2100 UTC, the rear inflow jet in the middle level disrupts the mid-tropospheric

updraft within the leading convection. The Morrison ABI MP dep. $\boldsymbol{r_e}$ experiment exhibits a stronger rear inflow jet at a lower level than the Morrison ABI const. $\boldsymbol{r_e}$, suggesting improvements in potential temperature related to latent cooling (Fig. 15d). Hence, the intensified low-level rear inflow jet at 2000 UTC sustains the leading convection's updraft at 2100 UTC.

Chapter 4

Conclusions

This study examines the impact of various microphysics parameterization schemes, and the consistency between their hydrometeor effective radii and that of the ABI observation operator, on the assimilation of GOES-16 ABI all-sky infrared BT for a typical bow echo case. In particular, their effects on the analysis and prediction of the bowing MCS reflectivity forecasts are comprehensively evaluated in order to assess the impacts of assimilating all-sky infrared BT on the internal dynamics of the bow echo.

As a first step to understand the impact of assimilating BT on the bowing MCS dynamics, this study shows that the correlation structures between BTs and model state variables are consistent with the role of vorticity augmentations and latent cooling (Fig. 16). Therefore, the assimilation of infrared BT can correct bowing MCS dynamics by updating the front-to-rear outflow, latent cooling, and rear inflow jet, even though infrared BT is mostly sensitive to hydrometeors near the cloud top.

In the DA experiments, this study tests four microphysics parameterization schemes: Thompson, NSSL, WDM6, and Morrison schemes. As the initial set of experiments, baseline experiments are performed for each microphysics scheme, assimilating conventional observations and radar reflectivity while excluding the assimilation of infrared BT. All baseline experiments result in a narrower simulated area of the rear inflow jet, leading to a reduced size of the bow echo and a corresponding narrower swath of surface severe winds compared to experiments with ABI assimilated. The baseline experiment utilizing strong latent cooling (e.g., WDM6 and Thompson)

demonstrates an earlier development of the bowing process compared to the baseline experiment with weaker latent cooling (e.g., NSSL and Morrison).

For each baseline experiment, a corresponding experiment (ABI const. $\boldsymbol{r_e}$) is performed by assimilating ABI infrared BT using a constant default effective radius for each hydrometeor type defined in the current GSI system. The purpose of these experiments is to investigate the impact of varying fall velocity assumptions and latent cooling, inherent in microphysics schemes, on the analysis increments associated with the dynamics of the bowing MCS. During DA cycling, the assimilation of BT primarily corrects the trailing stratiform region due to the greater sensitivity of ABI BT observations to smaller hydrometeor particles, which radar may not detect. Specifically, the experiments employing microphysics schemes with fast fall velocity assumptions (e.g., WDM6) and strong latent cooling (e.g., WDM6 and Thompson) result in more substantial accumulated impacts on the rear inflow jet, compared to schemes with slow fall velocity (e.g., Morrison) and weak latent cooling (e.g., NSSL and Morrison). Increasing the degree of impact on the rear inflow jet leads to a wider bow echo in the final analysis when assimilating BT. Consequently, the sizes of the analyzed bow echo follow the order of WDM6, Thompson, NSSL, and Morrison ABI const. $\boldsymbol{r_e}$ experiments. The wider bow echo size analyzed in each ABI const. $\boldsymbol{r_e}$ experiment persists throughout the forecast, leading to improved timing of the bowing process and a wider area of severe surface winds compared to their respective baselines.

An additional set of experiments (ABI MP dep. $\boldsymbol{r_e}$) is conducted, using the same DA design as ABI const. $\boldsymbol{r_e}$, but with microphysics-dependent effective radius calculated based on each microphysics scheme. The experiments aim to explore the impact of varying effective radius across microphysics schemes on prior BTs, BT innovations, and analysis increments associated with the dynamics of the bowing MCS. The utilization of the microphysics-dependent effective

radius has a significant impact primarily in the trailing stratiform region of the WDM6 and Morrison experiments due to prevalent optically thin ice particles than optically thick snow. Under low optical thickness conditions, using a microphysics-dependent effective radius larger than the constant default value for ice leads to higher prior BT and subsequent impact on the rear inflow jet during BT assimilation. During DA cycling, the significant impacts in the Morrison ABI MP dep. $\boldsymbol{r_e}$ experiment intensify the downward motion of the rear inflow jet, leading to improved timing of the bowing process and an enhanced forecast of MCV and corresponding severe surface winds. However, in the WDM6 MP dep. $\boldsymbol{r_e}$ experiment, the overestimation of the rear inflow jet intensity leads to the premature dissipation of the bowing MCS due to a possible shear imbalance between the environment and the cold pool (Rotunno et al. 1988). The overestimation of the rear inflow jet may be attributed to the strong latent cooling and fast ice fall velocity in the WDM6 scheme.

This study is the first to examine the influence of microphysics schemes on the assimilation of infrared BT and to enhance the consistency between microphysics schemes and the radiative transfer model by incorporating hydrometeor effective radius in the DA process. Further investigations should be conducted to assess the impact of these findings on additional severe weather events. This study highlights the importance of optimizing microphysics schemes to accurately simulate cloudy BT consistent with satellite observations. While bias correction of all-sky infrared radiances has shown improvement in convective scale DA (Otkin et al. 2018; Otkin and Pothast 2019; Johnson et al. 2022; Chandramouli et al. 2022), the optimal bias correction method remains an open question and may vary across different microphysics schemes. In this study, bias correction is not employed initially to gain a better understanding of the inherent biases in the microphysics-based prior BT. Future research should investigate how these findings interact

with bias correction methods suitable for each specific microphysics scheme. Future studies should focus on improving the consistency between microphysics schemes and radiative transfer models in infrared regimes, including particle size distribution, mass-diameter relation, non-spherical shape, and preferred orientation. Such consistency can be achieved by developing new look-up tables, similar to previous studies that focused on microwave channels (Sieron et al. 2017; Sieron et al. 2018; Moradi et al. 2022; Ren et al. 2023). To efficiently update various scales, it is recommended to consider the utilization of the multiscale data assimilation (MDA) method, as suggested in previous studies (Wang et al. 2020; Huang et al. 2020; Wang and Wang 2023). Future research in this field is anticipated to provide valuable insights into the assimilation of all-sky BT using multi-physics ensemble DA or stochastic physics parameterization.

References

Adams-Selin, R. D., S. C. van den Heever, and R. H. Johnson, 2013a: Impact of graupel parameterization schemes on idealized bow echo simulations. *Mon. Wea. Rev.*, 141, 1241–1262, https://doi.org/10.1175/MWR-D-12-00064.1

——, ——, and ——, 2013b: Sensitivity of bow-echo simulation to microphysical parameterizations. *Wea. Forecasting*, 28, 1188–1209, https://doi.org/10.1175/WAF-D-12-00108.1.

Atkins, N. T., J. M. Arnott, R. W. Przybylinski, R. A. Wolf, and B. D. Ketcham, 2004: Vortex structure and evolution within bow echoes. Part I: Single-Doppler and damage analysis of the 29 June 1998 derecho. *Mon. Wea. Rev.*, 132, 2224–2242, https://doi.org/10.1175/1520-0493(2004)132<2224:VSAEWB>2.0.CO;2.

——, and M. S. Laurent, 2009: Bow echo mesovortices. Part II: Their genesis. *Mon. Wea. Rev.*, 137, 1514–1532, https://doi.org/10.1175/2008MWR2650.1.

Bae, S. Y., S.-Y. Hong, and K. S. Lim, 2016: Coupling WRF double-moment 6-class microphysics schemes to RRTMG radiation scheme in Weather Research Forecasting model. *Adv. Meteor.*, 2016, 1–11, https://doi.org/10.1155/2016/5070154.

——, and R.-S. Park, 2019: Consistency between the cloud and radiation processes in a numerical forecasting model. *Meteor. Atmos. Phys.*, 131(5), 1429–1436, https://doi.org/10.1007/s00703-018-0647-9.

Baran, A. J., P. Hill, K. Furtado, P. Field, and J. Manners, 2014: A coupled cloud physics–radiation parameterization of the bulk optical properties of cirrus and its impact on the Met Office Unified Model Global Atmosphere 5.0 configuration. *J. Climate*, 27, 7725–7752, https://doi.org/10.1175/JCLI-D-13-00700.1.

Benjamin, S. G., and Coauthors, 2016: A North American hourly assimilation and model forecast cycle: The Rapid Refresh. *Mon. Wea. Rev.*, 144, 1669–1694, http://doi.org/10.1175/MWR-D-15-0242.1.

Chan, M.-Y., F. Q. Zhang, X. C. Chen, and L. R. Leung, 2020: Potential impacts of assimilating all-sky satellite infrared radiances on convection-permitting analysis and prediction of tropical convection. *Mon. Wea. Rev.*, 148, 3203−3224, https://doi.org/10.1175/MWR-D-19-0343.1.

Chandramouli, K., X. Wang, A. Johnson, and J. Otkin, 2022: Online nonlinear bias correction in ensemble Kalman filter to assimilate GOES-R all-sky radiances for the analysis and prediction of rapidly developing supercells. *J. Adv. Model. Earth Syst.*, 14, e2021MS002711, https://doi.org/10.1029/2021MS002711.

Chen, S., and W. R. Cotton, 1988: The sensitivity of a simulated extratropical mesoscale convective system to longwave radiation and ice-phase microphysics. *J. Atmos. Sci.*, 45, 3897-3910, https://doi.org/10.1175/1520-0469(1988)045<3897:TSOASE>2.0.CO;2.

Cintineo, R. M., J. A. Otkin, T. A. Jones, S. Koch, and D. J. Stensrud, 2016: Assimilation of synthetic GOES-R ABI infrared brightness temperatures and WSR-88D radar observations in a high-resolution OSSE. *Mon. Wea. Rev.*, 144, 3159−3180, https://doi.org/10.1175/MWR-D-15-0366.1.

Feng, Z., L. R. Leung, R. A. Houze, S. Hagos Jr., J. Hardin, Q. Yang, B. Han, and J. Fan, 2018: Structure and evolution of mesoscale convective systems: Sensitivity to cloud microphysics in convection-permitting simulations over the United States. *J. Adv. Model. Earth Syst.*, 10, 1470–1494, https://doi.org/10.1029/2018MS001305.

Fovell, R. G., and Y. Ogura, 1988: Numerical simulation of a midlatitude squall line in two dimensions. *J. Atmos. Sci.*, 45, 3846–3879, https://doi.org/10.1175/1520-0469(1988)045<3846:NSOAMS>2.0.CO;2.

Fu, Q., and K. N. Liou, 1993: Parameterization of the radiative properties of cirrus clouds. J. Atmos. Sci., 50, 2008–2025, https://doi.org/10.1175/1520-0469(1993)050<2008:POTRPO>2.0.CO;2.

Fujita, T. T., 1978: Manual of downburst identification for project Nimrod. Satellite and Mesometeorology Research Paper 156, Dept. of Geophysical Sciences, University of Chicago, 104 pp. [NTIS PB-286048.]

Gaspari, G., and S. E. Cohn, 1999: Construction of correlation functions in two and three dimensions. *Quart. J. Roy. Meteor. Soc.*, 125, 723–757, https://doi.org/10.1002/qj.49712555417.

Gasperoni, N. A., X. Wang, and Y. Wang, 2020: A comparison of methods to sample model errors for convection-allowing ensemble forecasts in the setting of multiscale initial conditions produced by the GSI-based EnVar assimilation system. *Mon. Wea. Rev.*, 148, 1177–1203, https://doi.org/10.1175/MWR-D-19-0124.1.

Griffin, S. M., and J. A. Otkin, 2022: Evaluating the impact of planetary boundary layer, land surface model, and microphysics parameterization schemes on simulated GOES-16 water vapor brightness temperatures. *Atmosphere*, 13, 366, https://doi.org/10.3390/atmos13030366.

Grim, J. A., G. M. McFarquhar, R. M. Rauber and B. F. Jewett, 2009a: Microphysical and thermodynamic structure and evolution of the trailing stratiform regions of mesoscale convective systems during BAMEX. Part II: Column model simulations. *Mon. Wea. Rev.*, 137, 1186-1205, https://doi.org/10.1175/2008MWR2505.1.

——, R. M. Rauber, G. M. McFarquhar, B. F. Jewett, and D. P. Jorgensen, 2009b: Development and forcing of the rear inflow jet in a rapidly developing and decaying squall line during BAMEX. *Mon. Wea. Rev.*, 137, 1206-1229, https://doi.org/10.1175/2008MWR2503.1.

Hamada, A., and Y. N. Takayabu, 2016: Convective cloud top vertical velocity estimated from geostationary satellite rapid-scan measurements. *Geophys. Res. Lett.*,43, 5435–5441, https://doi.org/10.1002/2016GL068962.

Han, Y., P. van Delst, Q. Liu, F. Weng, B. Yan, R. Treadon, and J. Derber, 2006: Community Radiative Transfer Model (CRTM): Version 1, NOAA technical report (p. 122). NOAA.

Honda, T., and Coauthors, 2018a: Assimilating all-sky Himawari-8 infrared radiances: A case of Typhoon Soudelor (2015). *Mon. Wea. Rev.*, 146, 213–229, https://doi.org/10.1175/MWR-D-16-0357.1.

——, S. Kotsuki, G.-Y. Lien, Y. Maejima, K. Okamoto, and T. Miyoshi, 2018b: Assimilation of Himawari-8 all-sky radiances every 10 minutes: Impact on precipitation and flood risk prediction. *J. Geophys. Res. Atmos.*, 123, 965–976, https://doi.org/10.1002/2017JD027096.

Huang, B., X. Wang, D. Kleist, and T. Lei, 2020: A Simultaneous Multi-scale Data Assimilation using Scale Dependent Localization in GSI-based Hybrid 4DEnVar for NCEP FV3-based GFS. *Mon. Wea. Rev.*, 149, 479-501, https://doi.org/10.1175/MWR-D-20-0166.1.

Hong, S.-Y., and J.-O. J. Lim, 2006: The WRF single-moment 6-class microphysics scheme (WSM6). *J. Korean Meteor. Soc.*, 42, 129–151.

Johnson, A., X. Wang, J. R. Carley, L. J. Wicker, and C. Karstens, 2015: A comparison of multiscale GSI-based EnKF and 3DVar data assimilation using radar and conventional observations for midlatitude convective-scale precipitation forecasts. *Mon. Wea. Rev.*, 143, 3087–3108, https://doi.org/10.1175/MWR-D-14-00345.1.

——, ——, T. A. Jones, 2022: Impacts of assimilating GOES-16 ABI channels 9 and 10 clear air and cloudy radiance observations with additive inflation and adaptive observation error in GSI-EnKF for a case of rapidly evolving severe supercells. *J. Geophys. Res. Atmos.*, 127, e2021JD036157, https://doi.org/10.1029/2021JD036157.

Jones, T. A., J. A. Otkin, D. J. Stensrud, and K. Knopfmeier, 2013: Assimilation of satellite infrared radiances and Doppler radar observations during a cool season observing system simulation experiment. *Mon. Wea. Rev.*, 141, 3273–3299, https://doi.org/10.1175/MWR-D-12-00267.1.

——, ——, ——, and ——, 2014: Forecast evaluation of an observing system simulation experiment assimilating both radar and satellite data. *Mon. Wea. Rev.*, 142, 107–124, https://doi.org/10.1175/MWR-D-13-00151.1.

——, P. Skinner, K. Knopmeier, E. Mansell, P. Minnis, R. Palikonda, and W. Smith Jr., 2018: Comparison of cloud microphysics schemes in a Warn-on-Forecast System using synthetic satellite objects. *Wea. Forecasting*, 33, 1681–1708, https://doi.org/10.1175/WAF-D-18-0112.1.

——, and Coauthors, 2020: Assimilation of GOES-16 radiances and retrievals into the Warn-on-Forecast System. *Mon. Wea. Rev.*, 148, 1829–1859, https://doi.org/10.1175/MWR-D-19-0379.1.

Kerr, C. A., D. J. Stensrud, and X. Wang, 2015: Assimilation of cloud-top temperature and radar observations of an idealized splitting supercell using an observing system simulation experiment. *Mon. Wea. Rev.*, 143, 1018−1034, https://doi.org/10.1175/MWR-D-14-00146.1.

Lafore, J.-P., and M. W. Moncrieff, 1989: A numerical investigation of the organization and interaction of the convective and stratiform regions of tropical squall lines. *J. Atmos. Sci.*, 46, 521–544, https://doi.org/10.1175/1520-0469(1989)046<0521:ANIOTO>2.0.CO;2.

Lim, K.-S. S., and S.-Y. Hong, 2010: Development of an Effective Double-Moment Cloud Microphysics Scheme with Prognostic Cloud Condensation Nuclei (CCN) for Weather and Climate Models. *Mon. Wea. Rev.*, 138, 1587-1612, https://doi.org/10.1175/2009MWR2968.1.

Liu, C., P. Yang, P. Minnis, N. Loeb, S. Kato, A. Heymsfield, and C. Schmitt, 2014: A two-habit model for the microphysical and optical properties of ice clouds. *Atmos. Chem. Phys.*, 14, 13,719–13,737, https://doi.org/10.5194/acp-14-13719-2014.

Mansell, E. R., C. L. Ziegler, and E. C. Bruning, 2010: Simulated electrification of a small thunderstorm with two-moment bulk microphysics. *J. Atmos. Sci.*, 67, 171–194, https://doi.org/10.1175/2009JAS2965.1.

McFarquhar, G. M., and A. J. Heymsfield, 1996: Microphysical characteristics of three anvils sampled during the Central Equatorial Pacific Experiment (CEPEX). *J. Atmos. Sci.*,53, 2401–2423, https://doi.org/10.1175/1520-0469(1996)053<2401:MCOTAS>2.0.CO;2.

——, and ——, 1998: The definition and significance of an effective radius for ice clouds. *J. Atmos. Sci.*, 55, 2039–2052, https://doi.org/10.1175/1520-0469(1998)055<2039:TDASOA>2.0.CO;2.

——, S. Iacobellis, and R. C. J. Somerville, 2003: SCM simulations of tropical ice clouds using observationally based parameterizations of microphysics. *J. Climate*, 16, 1643–1664, https://doi.org/10.1175/1520-0442(2003)016<1643:SSOTIC>2.0.CO;2.

Mitchell, D. L., P. Rasch, D. Ivanova, G. M. McFarquhar and T. Nousianen, 2008: The impact of controversial small ice crystals on GCM simulations. *Geophys. Res. Lett.*, 35, L09806, https://doi.org/10.1029/2008GL033552.

Minamide, M., and F. Zhang, 2017: Adaptive observation error inflation for assimilating all-sky satellite radiance. Mon. Wea. Rev., 145, 1063–1081, https://doi.org/10.1175/MWR-D-16-0257.1.

——, and ——, 2018: Assimilation of all-sky infrared radiances from Himawari-8 and impacts of moisture and hydrometer initialization on convection-permitting tropical cyclone prediction. *Mon. Wea. Rev.*, 146, 3241–3258, https://doi.org/10.1175/MWR-D-17-0367.1.

Mlawer, E. J., S. J. Taubman, P. D. Brown, M. J. Iacono, and S. A. Clough, 1997: Radiative transfer for inhomogeneous atmospheres: RRTM, a validated correlated-k model for the longwave. *J. Geophys. Res. Atmos.*, 102, 16663–16682, https://doi.org/10.1029/97JD00237.

Morrison, H., G. Thompson, and V. Tatarskii, 2009: Impact of cloud microphysics on the development of trailing stratiform precipitation in a simulated squall line: Comparison of one- and two-moment schemes. *Mon. Wea. Rev.*, 137, 991–1007, https://doi.org/10.1175/2008mwr2556.1.

Moradi, I., and Coauthors, 2022: Implementation of a discrete dipole approximation scattering database into community radiative transfer model. *J. Geophys. Res. Atmos.*, 127, e2022JD036957, https://doi.org/10.1029/2022JD036957.

Nakanishi, M., and H. Niino, 2009: Development of an improved turbulence closure model for the atmospheric boundary layer. *J. Meteor. Soc. Japan*, 87, 895–912, https://doi.org/10.2151/jmsj.87.895.

Niu, G.-Y., and Coauthors, 2011: The community Noah land surface model with multiparameterization options (Noah-MP): 1. Model description and evaluation with local-scale measurements, *J. Geophys. Res.*, 116, D12109, https://doi:10.1029/2010JD015139.

Otkin, J. A., 2012: Assimilation of water vapor sensitive infrared brightness temperature observations during a high impact weather event. *J. Geophys. Res.*, 117, D19203, https://doi.org/10.1029/2012JD017568.

——, R. Pothast, and A. S. Lawless, 2018: Nonlinear bias correction for satellite data assimilation using Taylor series polynomials. *Mon. Wea. Rev.*, 146, 263– 285, https://doi.org/10.1175/mwr-d-17-0171.1.

——, and ——, 2019: Assimilation of all-sky SEVIRI infrared brightness temperatures in a regional-scale ensemble data assimilation system. *Mon. Wea. Rev.*, 147, 4481– 4509, https://doi.org/10.1175/mwr-d-19-0133.1.

Pandya, R. E., and D. R. Durran, 1996: The influence of convectively generated thermal forcing on the mesoscale circulation around squall lines. *J. Atmos. Sci.*,53, 2924–2951, https://doi.org/10.1175/1520-0469(1996)053<2924:TIOCGT>2.0.CO;2.

——, ——, and M. L. Weisman, 2000: The influence of convective thermal forcing on the three-dimensional circulation around squall lines. *J. Atmos. Sci.*, 57, 29–45, https://doi.org/10.1175/1520-0469(2000)057<0029:TIOCTF>2.0.CO;2.

Parol, F., J. C. Buriez, G. Brogniez, and Y. Fouquart, 1991: Information content of AVHRR channels 4 and 5 with respect to the effective radius of cirrus cloud particles. *J. Appl. Meteor.*,30, 973–984, https://doi.org/10.1175/1520-0450-30.7.973.

Prabhakara, C., R. S. Fraser, G. Dalu, M.-L. Wu, R. J. Curran, and T. Styles, 1988: Thin cirrus clouds: Seasonal distribution over oceans deduced from Nimbus-4 IRIS. J. Appl. Meteor.,27, 379–399, https://doi.org/10.1175/1520-0450(1988)027<0379:TCCSDO>2.0.CO;2.

Przybylinski, R. W., 1995: The bow echo: Observations, numerical simulations, and severe weather detection methods. *Wea. Forecasting*, 10, 203–218, https://doi.org/10.1175/1520-0434(1995)010<0203:TBEONS>2.0.CO;2.

Ren, T., P. Yang, K. Garrett, Y. Ma, J. Ding, and J. Coy, 2023: A Microphysics-Scheme-Consistent Snow Optical Parameterization for the Community Radiative Transfer Model. *Mon. Wea. Rev.*, 151, 383-402, https://doi.org/10.1175/MWR-D-22-0145.1.

Roberts, N. M., and H. W. Lean, 2008: Scale-selective verification of rainfall accumulations from high-resolution forecasts of convective events. *Mon. Wea. Rev.*, 136, 78–97, https://doi.org/10.1175/2007MWR2123.1.

Schiemann, R., P. L. Vidale, L. C. Shaffrey, S. J. Johnson, M. J. Roberts, M.-E. Demory, M. S. Mizielinski, and J. Strachan, 2018: Mean and extreme precipitation over European river basins better simulated in a 25 km AGCM. *Hydrol. Earth Syst. Sci.*, 22, 3933–3950, https://doi.org/10.5194/hess-22-3933-2018.

Sieron, S. B., E. E. Clothiaux, F. Zhang, Y. Lu, and J. A. Otkin, 2017: Comparison of using distribution-specific versus effective radius methods for hydrometeor single-scattering properties for all-sky microwave satellite radiance simulations with different microphysics parameterization schemes. *J. Geophys. Res. Atmos.*,122, 7027–7046, https://doi.org/10.1002/2017JD026494.

——, F. Zhang, E. E. Clothiaux, L. N. Zhang, and Y. Lu, 2018: Representing precipitation ice species with both spherical and nonspherical particles for radiative transfer modeling of microphysics-consistent cloud microwave scattering properties. *J. Adv. Model. Earth Syst.*,10, 1011–1028, https://doi.org/10.1002/2017MS001226.

Skamarock, W. C, and Coauthors, 2021: A Description of the Advanced Research WRF Model Version 4.3 (No. NCAR/TN-556+STR), https://doi.org/10.5065/1dfh-6p97.

Smull, B. F., and R. A. Houze Jr., 1985: A midlatitude squall line with a trailing region of stratiform rain: Radar and satellite observations. *Mon. Wea. Rev.*, 113, 117–133, https://doi.org/10.1175/1520-0493(1985)113<0117:AMSLWA>2.0.CO;2.

——, and ——, 1987: Rear inflow in squall lines with trailing stratiform precipitation. *Mon. Wea. Rev.*, 115, 2869–2889, https://doi.org/10.1175/1520-0493(1987)115<2869:RIISLW>2.0.CO;2.

Stephens, G. L., 1978: Radiation profiles in extended water clouds, II, Parameterization schemes, *J. Atmos. Sci.*,35, 2123–2132, https://doi.org/10.1175/1520-0469(1978)035<2123:RPIEWC>2.0.CO;2.

Szeto, K. K., and H. Cho, 1994: A numerical investigation of squall lines. Part III: Sensitivity to precipitation processes and the Coriolis force. *J. Atmos. Sci.*, 51, 1341–1351, https://doi.org/10.1175/1520-0469(1994)051<1341:ANIOSL>2.0.CO;2.

Thompson, G., P. R. Field, R. M. Rasmussen, and W. D. Hall, 2008: Explicit forecasts of winter precipitation using an improved bulk microphysics scheme. Part II: Implementation of a new snow parameterization. *Mon. Wea. Rev.*, 136, 5095–5115, https://doi.org/10.1175/2008MWR2387.1.

——, M. Tewari, K. Ikeda, S. Tessendorf, C. Weeks, J. Otkin, and F. Kong, 2016: Explicitly-coupled cloud physics and radiation parameterizations and subsequent evaluation in WRF high-resolution convective forecasts. *Atmos. Res.*, 168, 92–104, https://doi.org/10.1016/j.atmosres.2015.09.005.

Trapp, R. J., and M. L. Weisman, 2003: Low-level mesovortices within squall lines and bow echoes. Part II: Their genesis and implications. *Mon. Wea. Rev.*, 131, 2804–2823, https://doi.org/10.1175/1520-0493(2003)131<2804:LMWSLA>2.0.CO;2.

Van Weverberg, K., and Coauthors, 2013: The role of cloud microphysics parameterization in the simulation of mesoscale convective system clouds and precipitation in the tropical western *Pacific. J. Atmos. Sci.*, 70, 1104–1128, https://doi.org/10.1175/JAS-D-12-0104.1.

Wang, X., D. Parrish, D. Kleist, and J. Whitaker, 2013: GSI 3DVar-based ensemble-variational hybrid data assimilation for NCEP Global Forecast System: Single-resolution experiments. *Mon. Wea. Rev.*, 141, 4098–4117, https://doi.org/10.1175/MWR-D-12-00141.1.

——, and T. Lei, 2014: GSI-based four-dimensional ensemble-variational (4DßEnsVar) data assimilation: Formulation and single-resolution experiments with real data for NCEP Global Forecast System. *Mon. Wea. Rev.*, 142, 3303–3325, https://doi.org/10.1175/MWR-D-13-00303.1.

——, H. G. Chipilski, C. H. Bishop, E. Satterfield, N. Baker, J. Whittaker, 2020: A Multiscale Local Gain Form Ensemble Transform Kalman Filter (MLGETKF). *Mon. Wea. Rev.*, 149, 605-622, https://doi.org/10.1175/MWR-D-20-0290.1.

Wang, Y., and X. Wang, 2017: Direct assimilation of radar reflectivity without tangent linear and adjoint of the nonlinear observation operator in the GSI-based EnVar system: Methodology and experiment with the 8 May 2003 Oklahoma City tornadic supercell. *Mon. Wea. Rev.*, 145, 1447–1471, https://doi.org/10.1175/MWR-D-16-0231.1.

——, and ——, 2023: Simultaneous multiscale data assimilation using scale- and variable-dependent localization in EnVar for convection allowing analyses and forecasts: Methodology and experiments for a tornadic supercell. *J. Adv. Model. Earth Syst.*, 15, e2022MS003430. https://doi.org/10.1029/2022MS003430.

Wang, Y., H. Su, J. H. Jiang, F. Xu, and Y. L. Yung, 2020: Impact of cloud ice particle size uncertainty in a climate model and implications for future satellite missions. *J. Geophys. Res. Atmos.*,125, e2019JD032119, https://doi.org/10.1029/2019JD032119.

Weisman, M. L, 1992: The role of convectively generated rear-inflow jets in the evolution of long-lived mesoconvective systems. *J. Atmos. Sci.*, 49, 1826–1847, https://doi.org/10.1175/1520-0469(1992)049<1826:TROCGR>2.0.CO;2.

Wheatley, D. M., R. J. Trapp, and N. T. Atkins, 2006: Radar and damage analysis of severe bow echoes observed during BAMEX. *Mon. Wea. Rev.*, 134, 791–806, https://doi.org/10.1175/MWR3100.1.

——, N. Yussouf, and D. J. Stensrud, 2014: Ensemble Kalman filter analyses and forecasts of a severe mesoscale convective system using different choices of microphysics schemes. *Mon. Wea. Rev.*, 142, 3243–3263, https://doi:10.1175/MWR-D-13-00260.1.

Whitaker, J. S., T. M. Hamill, X. Wei, Y. Song, and Z. Toth, 2008: Ensemble data assimilation with the NCEP global forecast system. *Mon. Wea. Rev.*, 136, 463–448, https://doi.org/10.1175/2007MWR2018.1.

——, and T. M. Hamill, 2012: Evaluating methods to account for system errors in ensemble data assimilation. *Mon. Wea. Rev.*, 140, 3078–3089, https://doi.org/10.1175/MWR-D-11-00276.1.

Zhang, F., M. Minamide, and E. E. Clothiaux, 2016: Potential impacts of assimilating all-sky infrared satellite radiance from GOES-R on convection-permitting analysis and prediction of tropical cyclones. *Geophys. Res. Lett.*, 43, 2954–2963, https://doi.org/10.1002/2016GL068468.

Zhang, J., and Coauthors, 2016: Multi-Radar Multi-Sensor (MRMS) quantitative precipitation estimation: Initial operating capabilities. *Bull. Amer. Meteor. Soc.*, 97, 621–638, https://doi.org/10.1175/BAMS-D-14-00174.1.

Zhang, Y., F. Zhang, and D. J. Stensrud, 2018: Assimilating all-sky infrared radiances from GOES-16 ABI using an ensemble Kalman filter for convection-allowing severe thunderstorms prediction. *Mon. Wea. Rev.*, 146, 3363–3381, https://doi.org/10.1175/MWR-D-18-0062.1.

——, E. E. Clothiaux, and D. J. Stensrud, 2022: Correlation structures between satellite all-sky infrared brightness temperatures and the atmospheric state at storm scales. *Adv. Atmos. Sci.*, 39(5), 714−732, https://doi.org/10.1007/s00376-021-0352-3.

Zhou, X., Y. Zhu, D. Hou, Y. Luo, J. Peng, and R. Wobus, 2017: Performance of the new NCEP global ensemble forecast system in a parallel experiment. *Wea. and Forecasting*, 32, 1989–2004, https://doi.org/10.1175/WAF-D-17-0023.1.

Zhu, L., M. Xue, R. Kong, and J. Min, 2023: Direct Assimilation of All-Sky GOES-R ABI Radiances in GSI EnKF for the Analysis and Forecasting of a Mesoscale Convective System. *Mon. Wea. Rev.*, 151, 737-760, https://doi.org/10.1175/MWR-D-21-0293.1.

Xu, X., M. Xue, and Y. Wang, 2015: Mesovortices within the 8 May 2009 bow echo over central United States: Analyses of the characteristics and evolution based on Doppler radar observations and a high-resolution model simulation. *Mon. Wea. Rev.*, 143, 2266-2290, https://doi.org/10.1175/MWR-D-14-00234.1.

Tables

Table 1. WRF model configurations

Resolution	3-km / 51 vertical layers up to 50 hPa
Time interval	20 secs
Microphysics	Thompson[a] / NSSL[b] / WDM6[c] / Morrison[d]
Cumulus	None
Radiation	RRTMG[e]
PBL	Mellor–Yamada–Nakanishi–Niino[f]
Surface / Land	Noah land surface model[g]

[a] Thompson et al. (2008)

[b] Mansell et al. (2010)

[c] Lim and Hong (2010)

[d] Morrison et al. (2009)

[e] Mlawer et al. (1997)

[f] Nakanishi and Niino (2009)

[g] Niu et al. (2011)

Table 2. Prior brightness temperature and latent cooling characteristics for microphysics parameterization schemes compared to the Thompson scheme.

	Thompson	**NSSL**	**WDM6**	**Morrison**
Prior brightness temperature	-	comparable[a]	higher[b]	lower[b,c]
Latent cooling within stratiform cloud	-	weaker[d]	stronger[e]	weaker[c]

[a] Jones et al. (2018)

[b] Van Weverberg et al. (2013)

[c] Feng et al. (2018)

[d] Wheatley et al. (2014)

[e] Adams-Selin et al. (2013b)

Table 3. Experiment design

Experiment	**Description**	**Purpose**
Baseline	No assimilation of BT	capability of each microphysics scheme in simulating the bowing process
ABI const. r_e	ABI all-sky infrared BT assimilation using **constant default effective radius**	impact of **hydrometeor fall velocity** and **latent cooling**
ABI MP dep. r_e	ABI all-sky infrared BT assimilation using **microphysics-dependent effective radius**	impact of hydrometeor **effective radius**

Figures

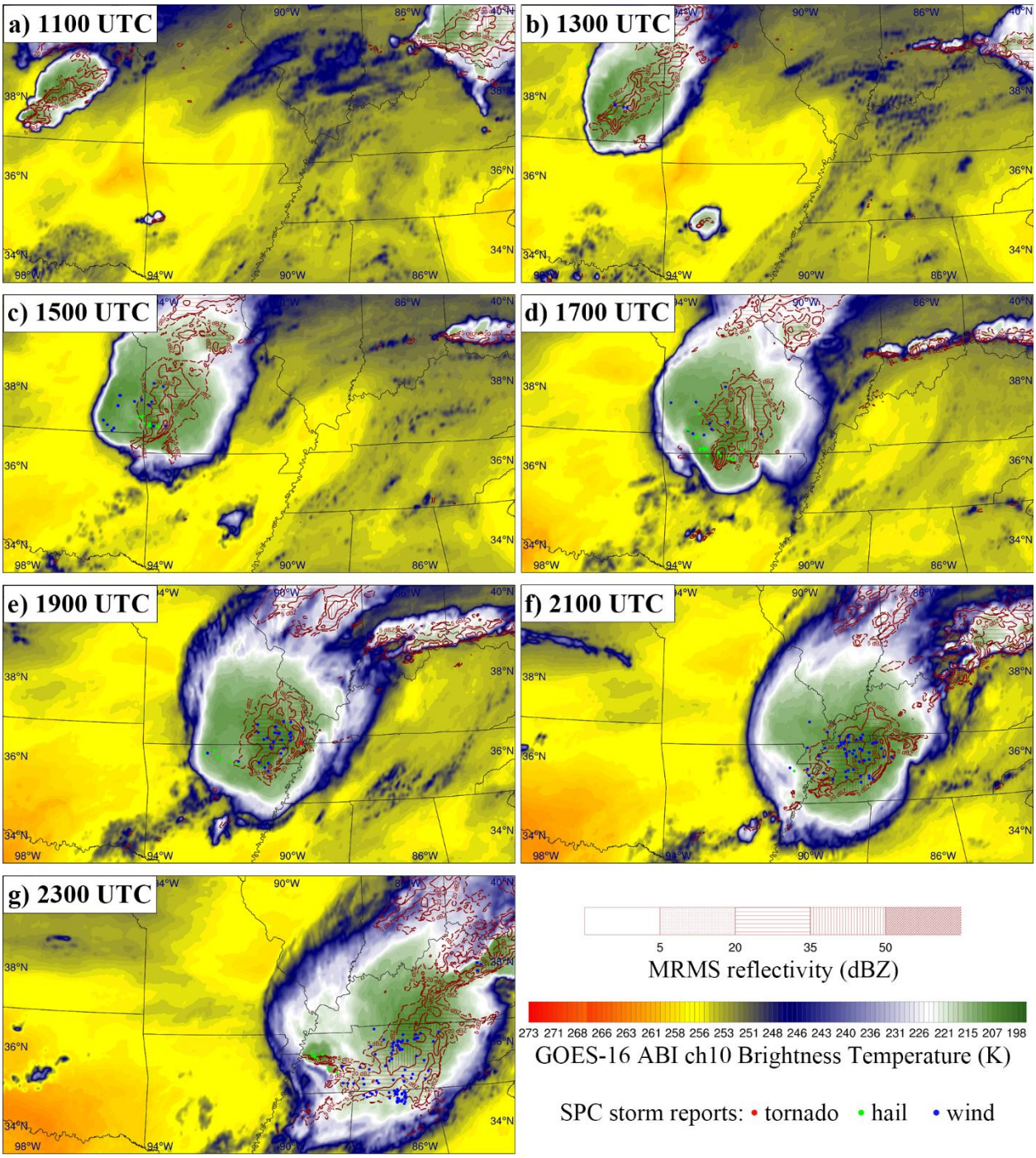

Fig. 1. GOES-16 ABI channel 10 brightness temperature (K, shaded), MRMS radar reflectivity 2-km AGL (dBZ, red filled lines), and SPC storm reports (tornadoes: red dots, hail: green dots, and wind: blue dots) for -2 – 0 hours from 1100 UTC to 2300 UTC 3 May 2020.

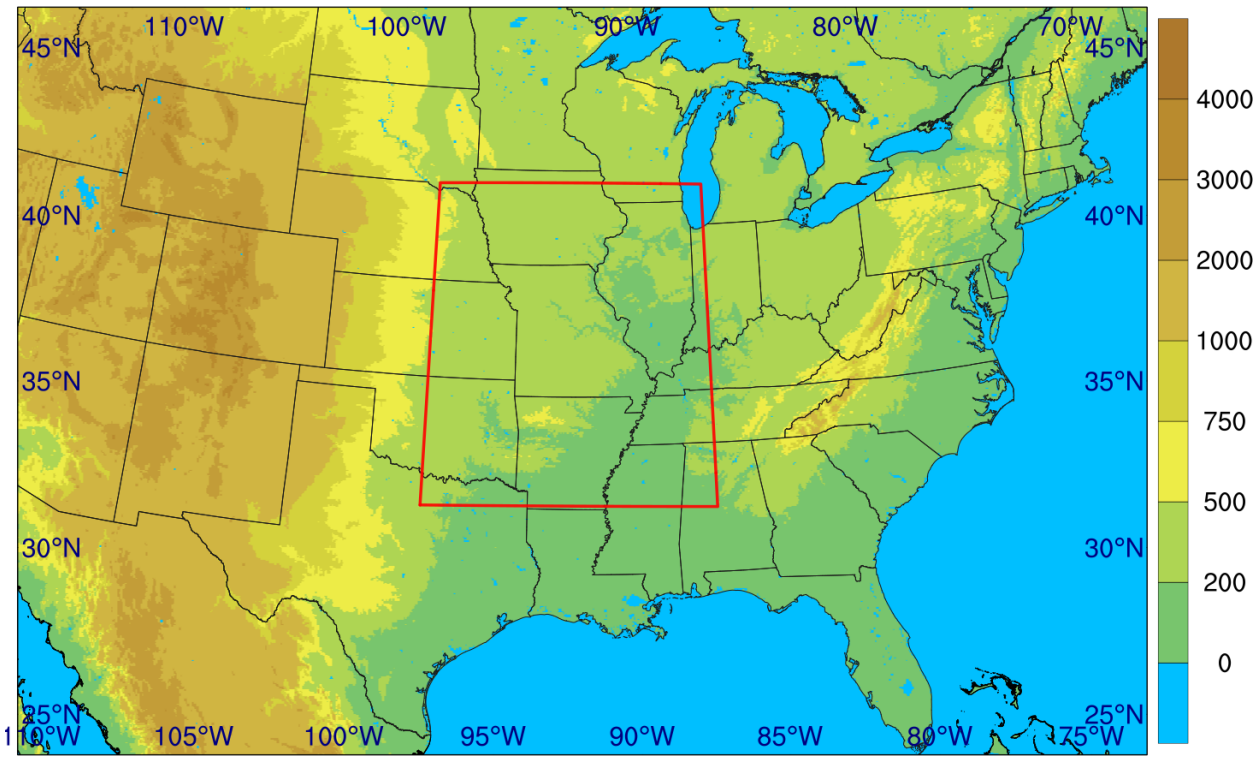

Fig. 2. WRF model domain (whole area), terrain height (shaded, m) and domain of interest (red box) where the GOES-16 ABI level 1 radiance observations are thinned from their original 2km resolution to a 6 km resolution. Outside the region of interest, the BTs are thinned to a 12 km resolution.

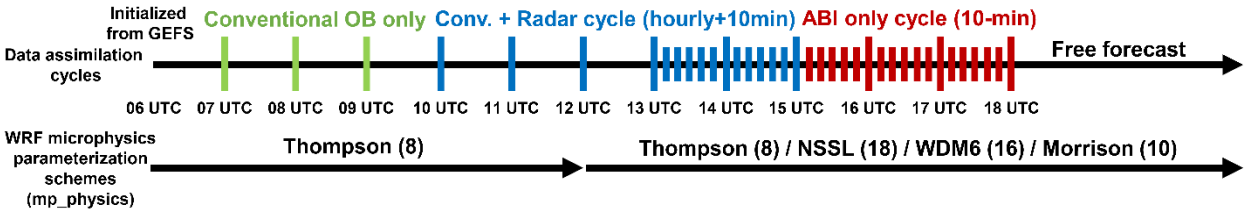

Fig. 3. Data assimilation cycles and microphysics parameterization schemes used in each cycle.

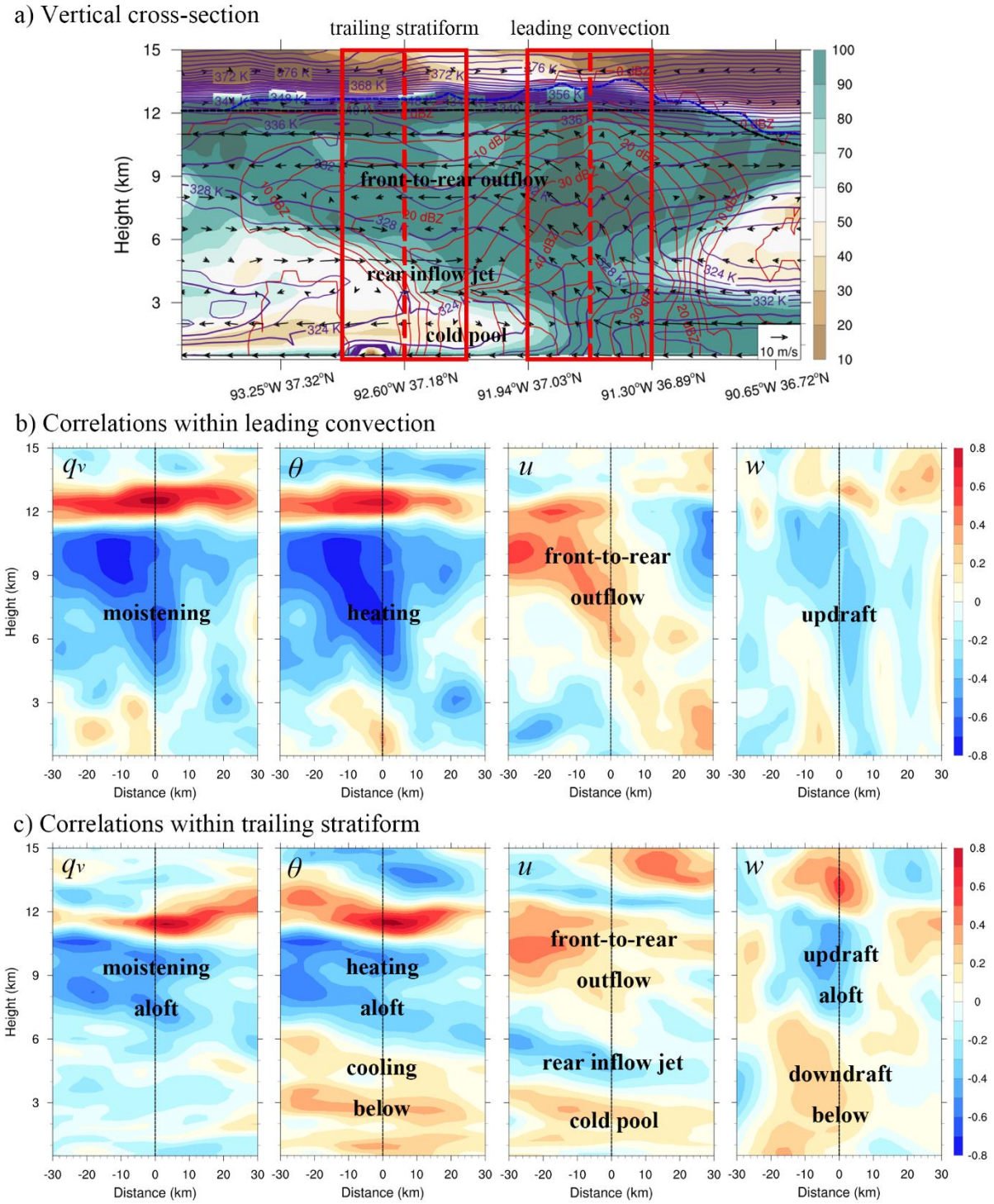

Fig. 4. Bowing MCS dynamics shown in a) cross-section of relative humidity (%, shaded), equivalent potential temperature (K, purple lines), reflectivity (dBZ, red lines), and wind along storm motion (vectors) in ensemble analysis mean at 1700 UTC and correlation structures between infrared brightness temperature and model state variables including water vapor mixing ratio (q_v). potential temperature (θ), horizontal wind along the storm motion (u), and vertical wind (w) within b) leading convection and c) trailing stratiform.

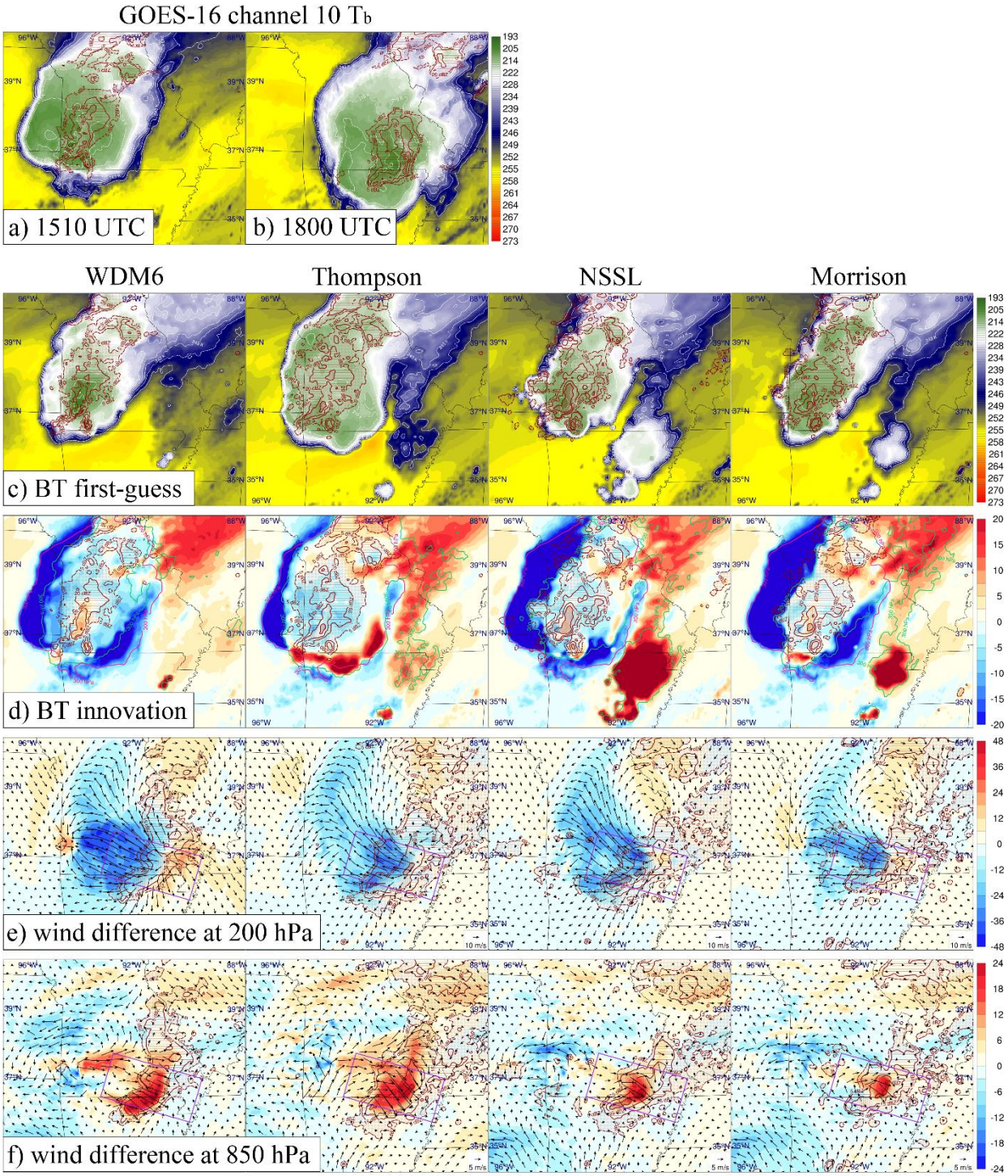

Fig. 5. GOES-16 ABI channel 10 brightness temperature (K) at a) 1510 UTC and b) 1800 UTC. c) prior brightness temperature (K) at 1510 UTC. d) brightness temperature innovation (observation minus first-guess, K) at 1510 UTC. Horizontal wind differences (m s^{-1}) between ABI constant default effective radius and baseline experiment (ABI const. $\boldsymbol{r_e}$ minus Baseline) along storm motion at e) 200 hPa and f) 850 hPa.

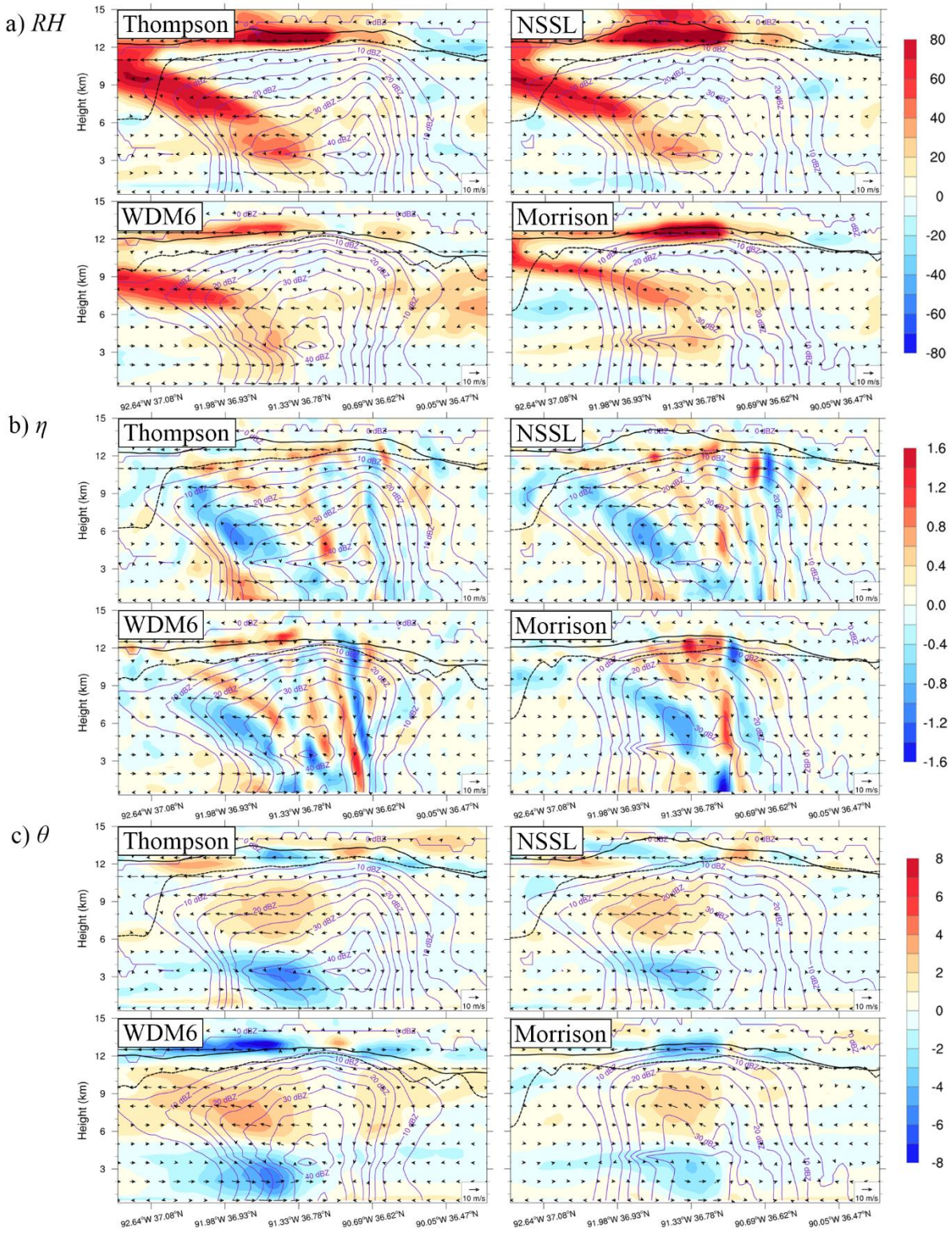

Fig. 6. Cross-sections of analysis differences between ABI constant effective radius and baseline experiments (ABI const. $\boldsymbol{r_e}$ minus Baseline) along storm motion in a) relative humidity (*RH*, %), b) horizontal vorticity (η, 10^{-3} s^{-1}), and c) potential temperature (θ, K), overlaid with analyzed reflectivity (purple lines, dBZ) and wind difference (vector).

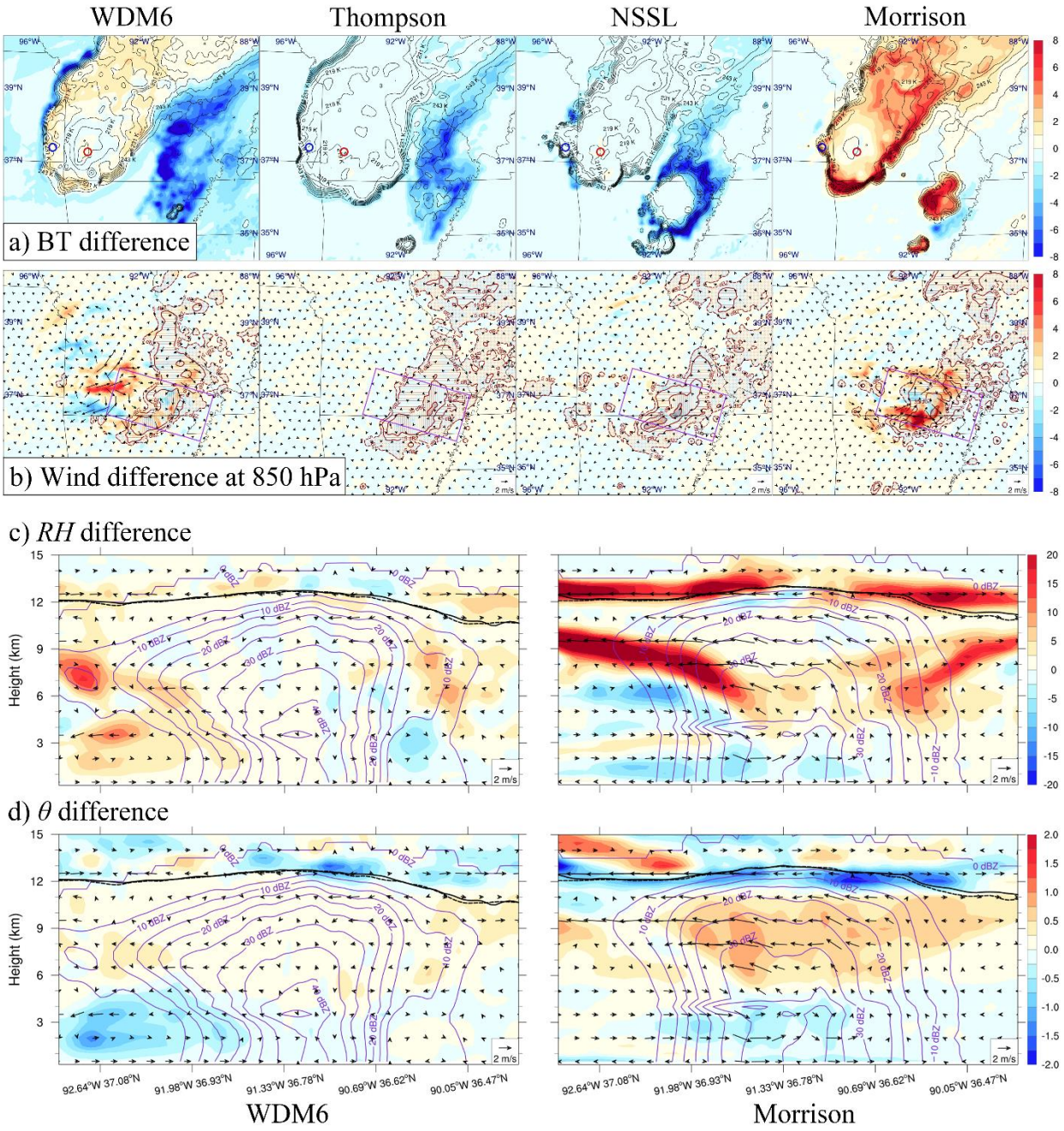

Fig. 7. Horizontal difference between ABI MP dep. $\boldsymbol{r_e}$ and ABI const. $\boldsymbol{r_e}$ experiments in a) prior brightness temperature (K) at 1510 UTC, b) 850 hPa wind (m s^{-1}) at 1800 UTC. Vertical difference between ABI MP $\boldsymbol{r_e}$ and ABI const. $\boldsymbol{r_e}$ experiments along cross-section in c) relative humidity (*RH*, %), and d) potential temperature (θ, K).

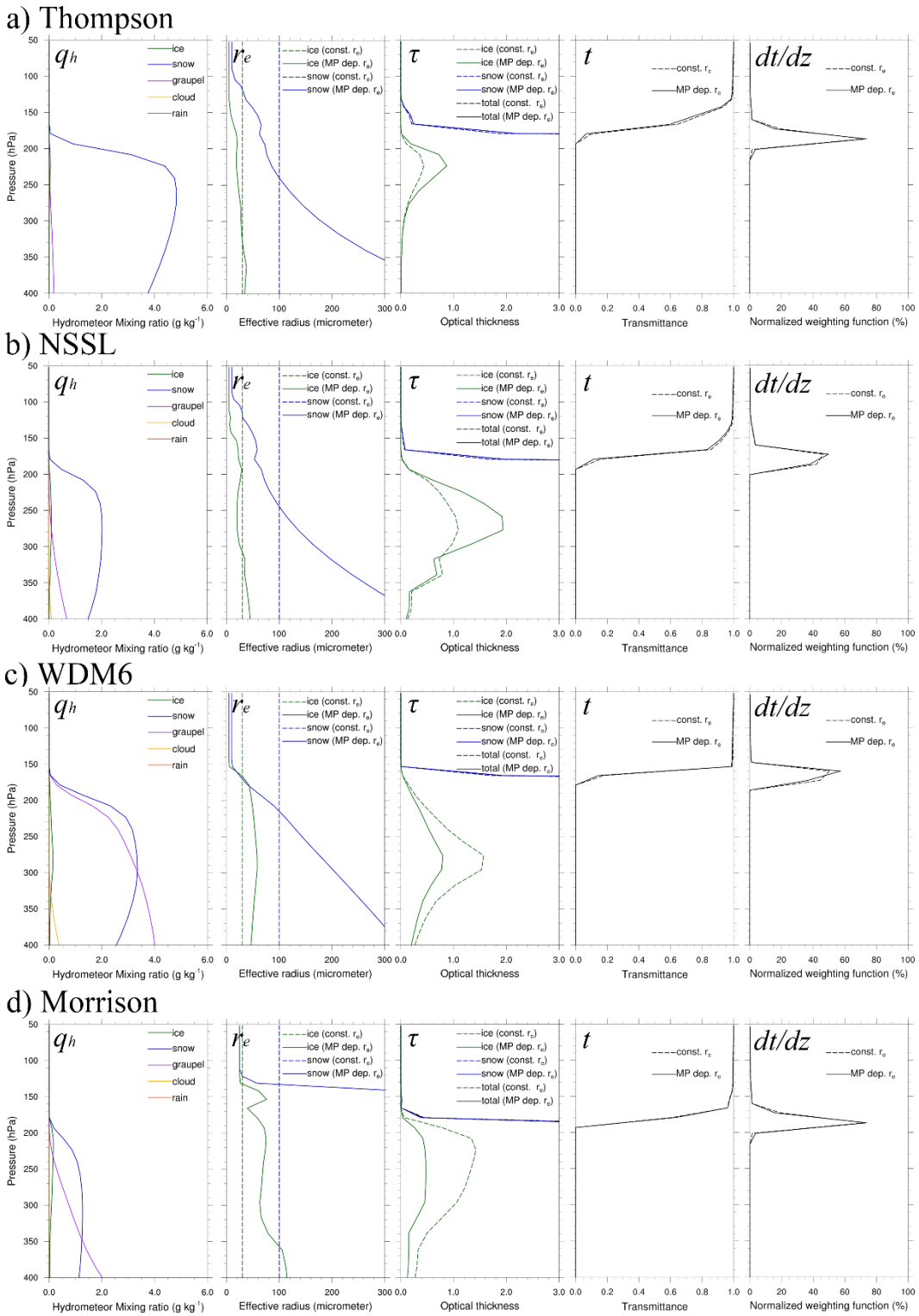

Fig. 8. Vertical profiles of hydrometeor mixing ratio (g kg^{-1}), effective radius (μm), optical thickness, transmittance, and normalized weighting function for a) Thompson, b) NSSL, c) WDM6, and d) Morrison schemes at the leading convection (95.018^{o}S 37.400^{o}N, red circle in Fig. 7a). As the effective radius in look-up table ranges from 2 μm to 100 μm, the constant default effective radius for snow is considered as 100 μm.

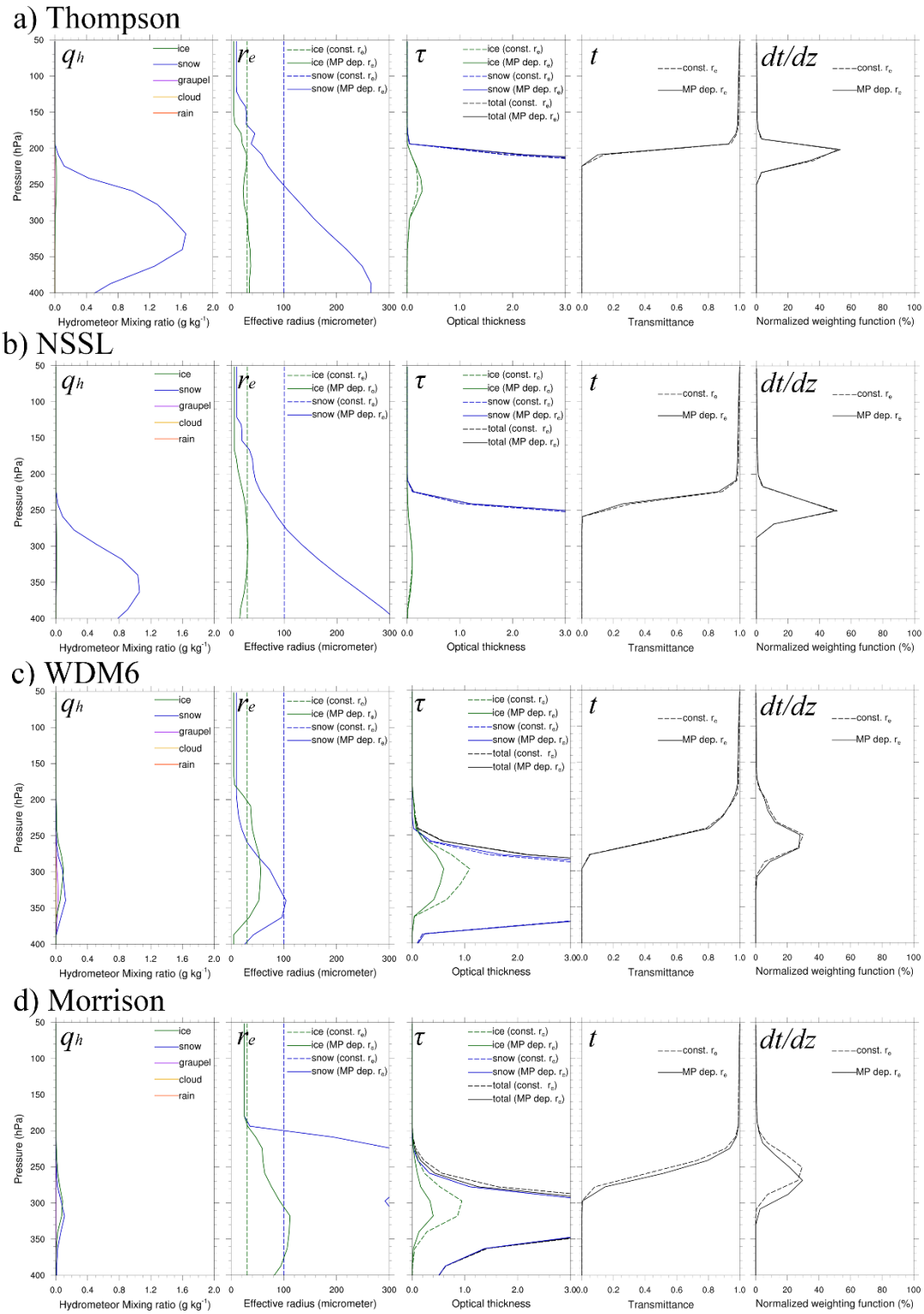

Fig. 9. Same as Fig. 8 but at the trailing stratiform cloud (94.530°S 36.369°N, blue circle in Fig. 7a).

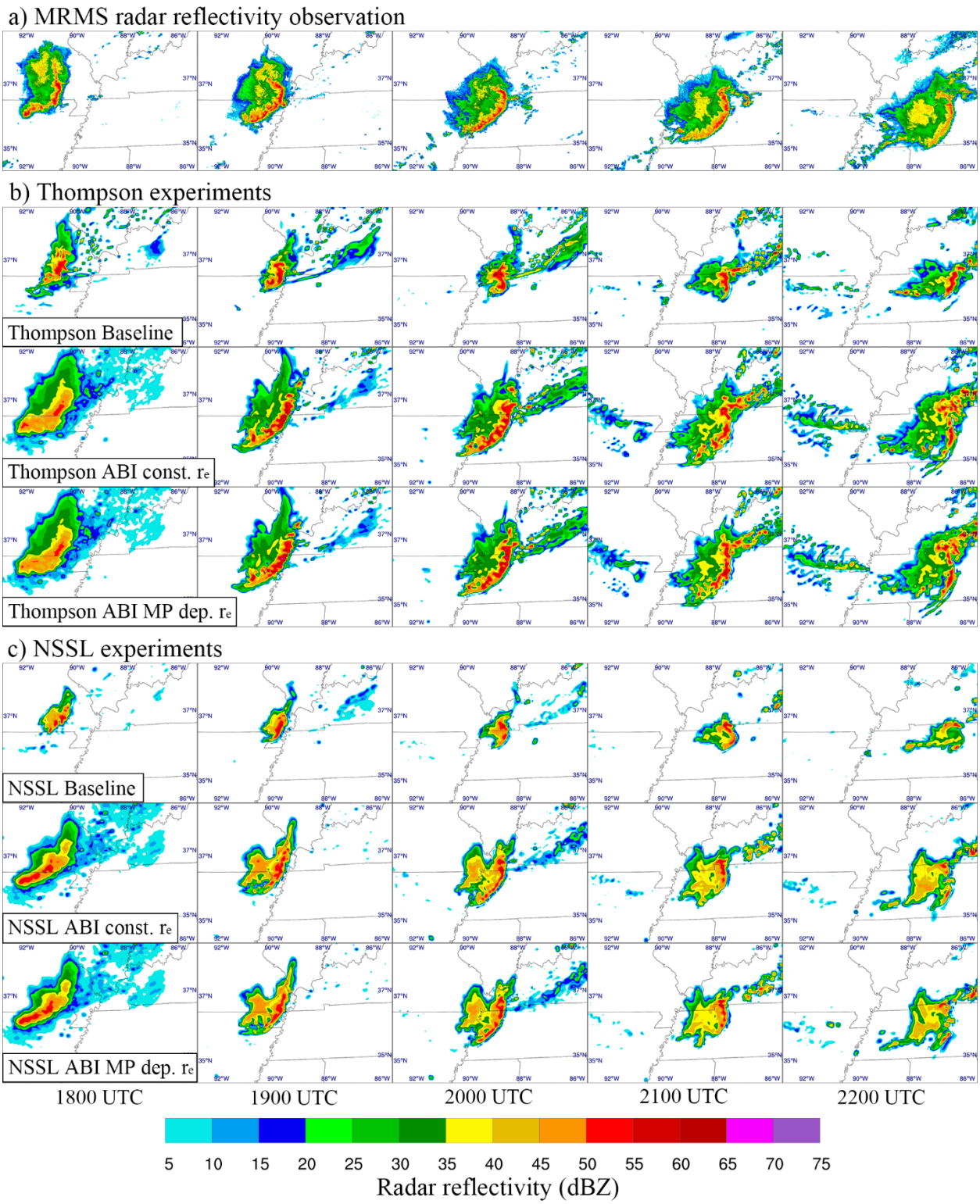

Fig. 10. a) MRMS radar reflectivity (dBZ) at 2 km AGL. Baseline, ABI const. $\boldsymbol{r_e}$, and ABI MP dep. $\boldsymbol{r_e}$ experiments using b) Thompson and c) NSSL microphysics schemes.

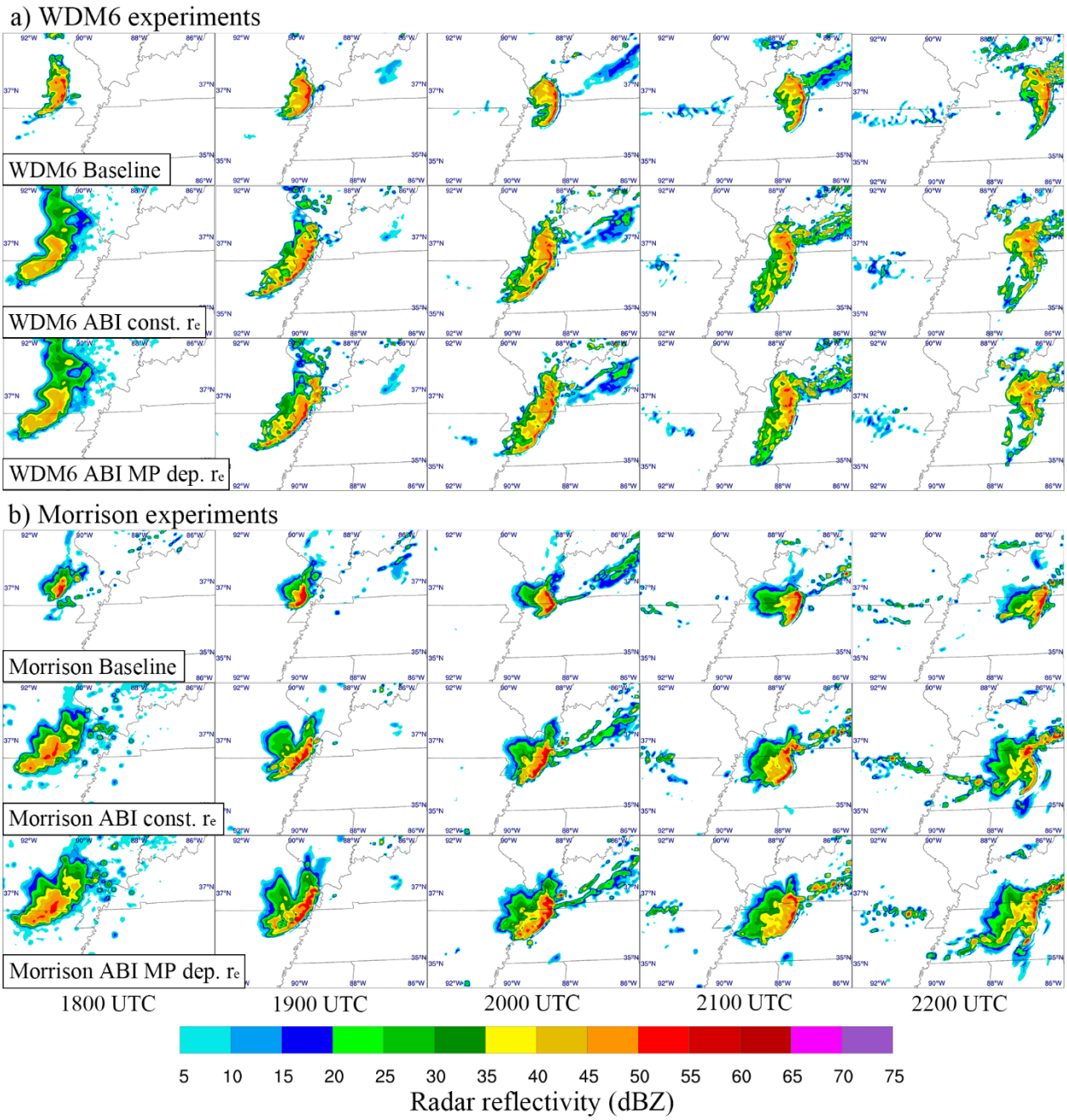

Fig. 11. Same as Fig. 10b and 10c, but experiments using a) WDM6 and b) Morrison microphysics schemes.

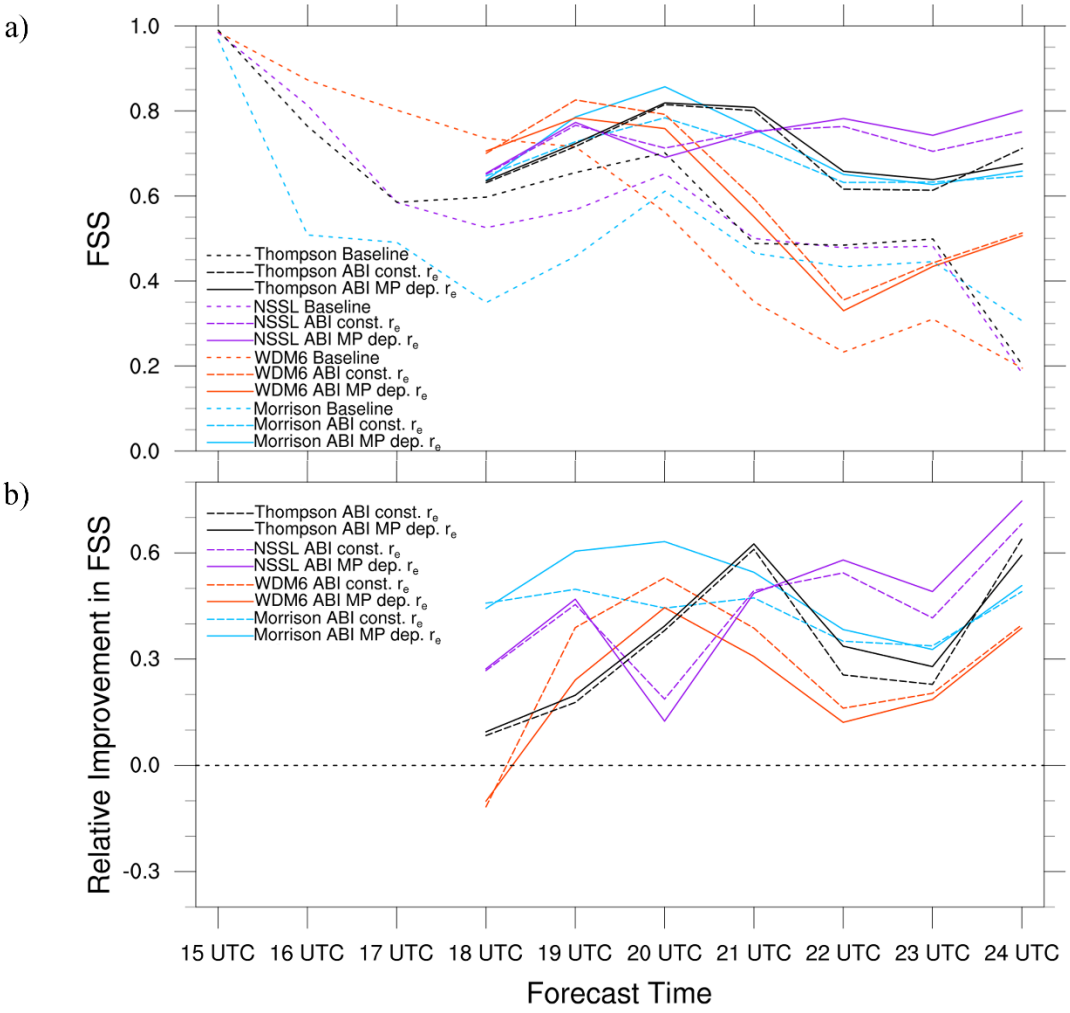

Fig. 12. Reflectivity verification using a) fractions skill score and b) relative improvement in fractions skill score.

a) SPC wind reports

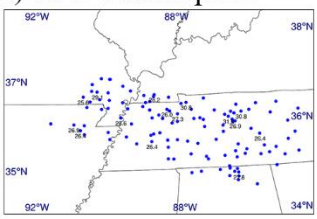

b) Simulated maximum wind at 10 m

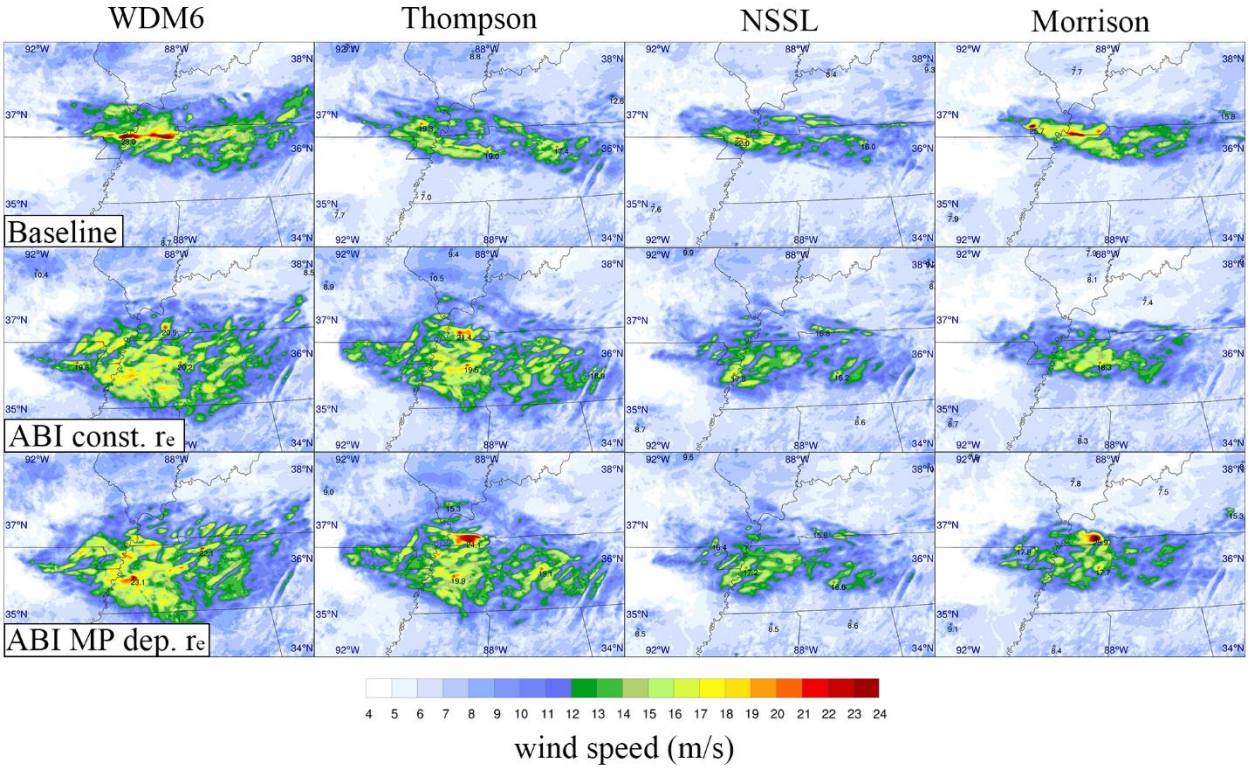

Fig. 13. Verification of surface severe winds (m s^{-1}). a) SPC wind reports and b) simulated maximum wind speeds at 10 m for 1800 – 0000 UTC.

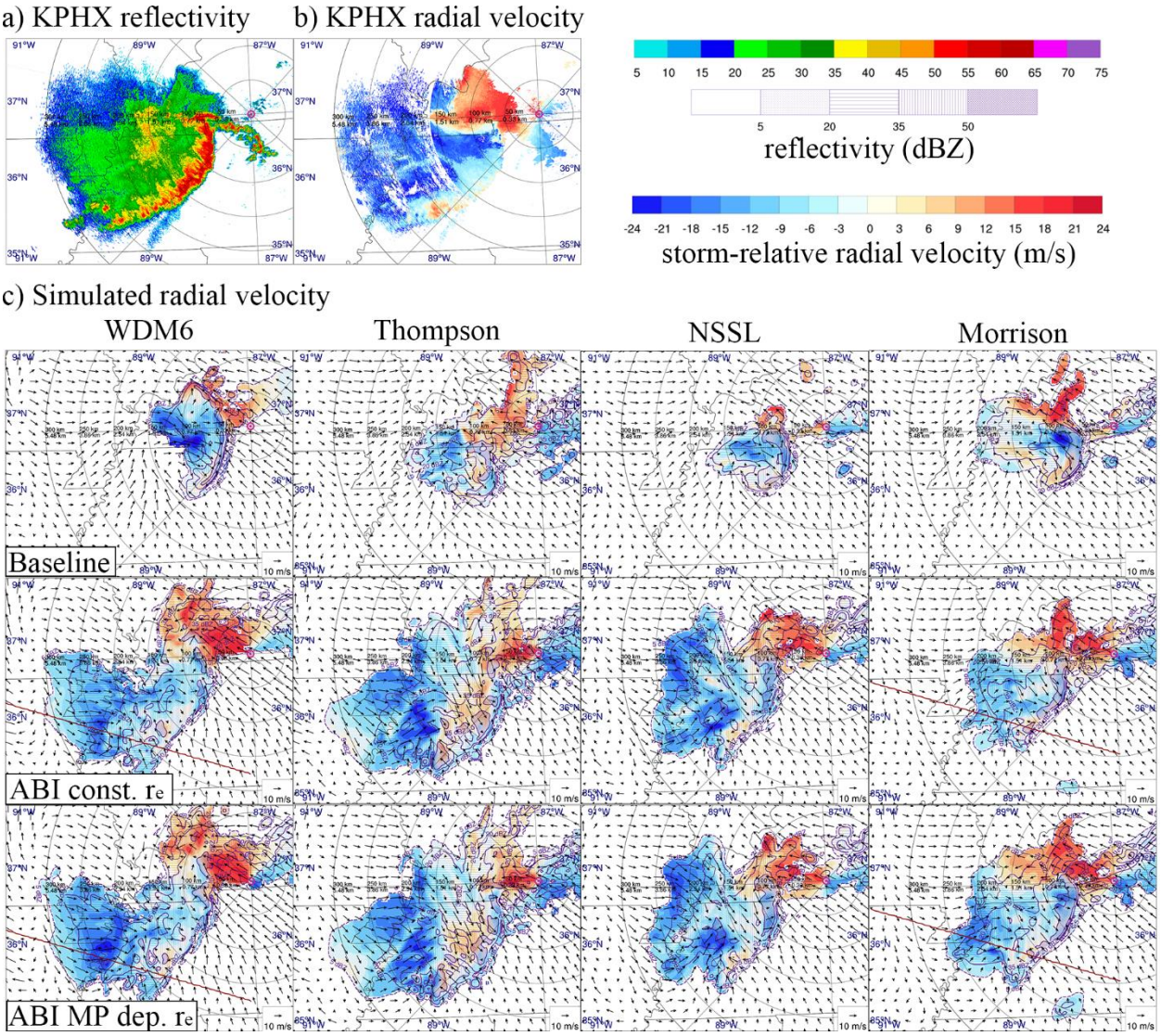

Fig. 14. KPHX radar observations at 2030 UTC of a) reflectivity (dBZ) and b) storm-relative radial velocity (m s^{-1}). c) simulated storm-relative radial velocity (m s^{-1}) of each experiment on the PPI plane at the elevation angle of 0.48 with radar site marked with magenta cycle.

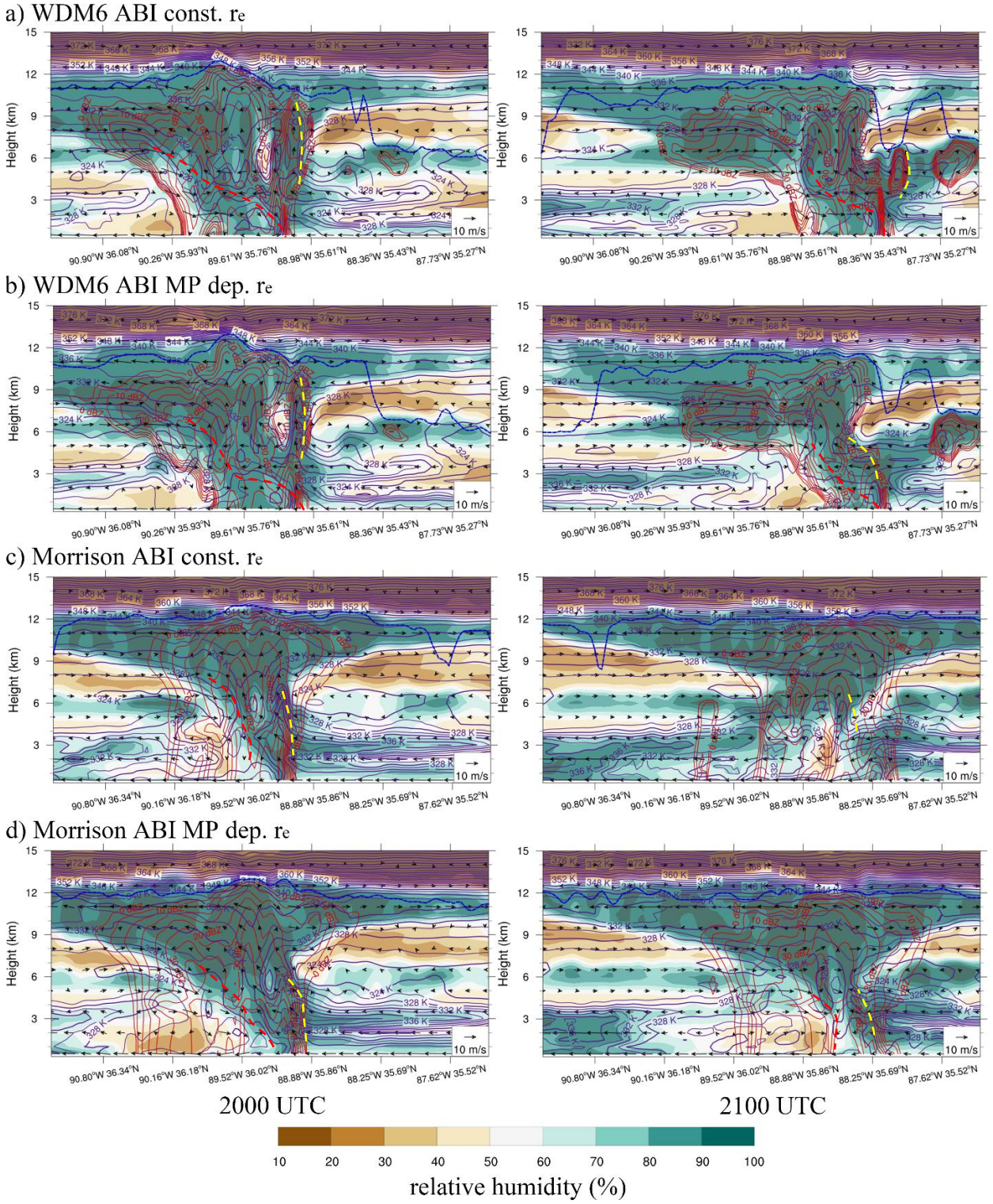

Fig. 15. Vertical cross-sections of relative humidity (%, shaded), reflectivity (dBZ, red solid lines), equivalent potential temperature (K, purple solid lines), and cloud top height (blue dashed line) along the red lines in Fig. 14b,c at the 2000 (left) and 2100 UTC (right) forecasts. The boundaries of rear inflow jet (red dashed line) and leading convection (yellow dashed line) are overlaid.

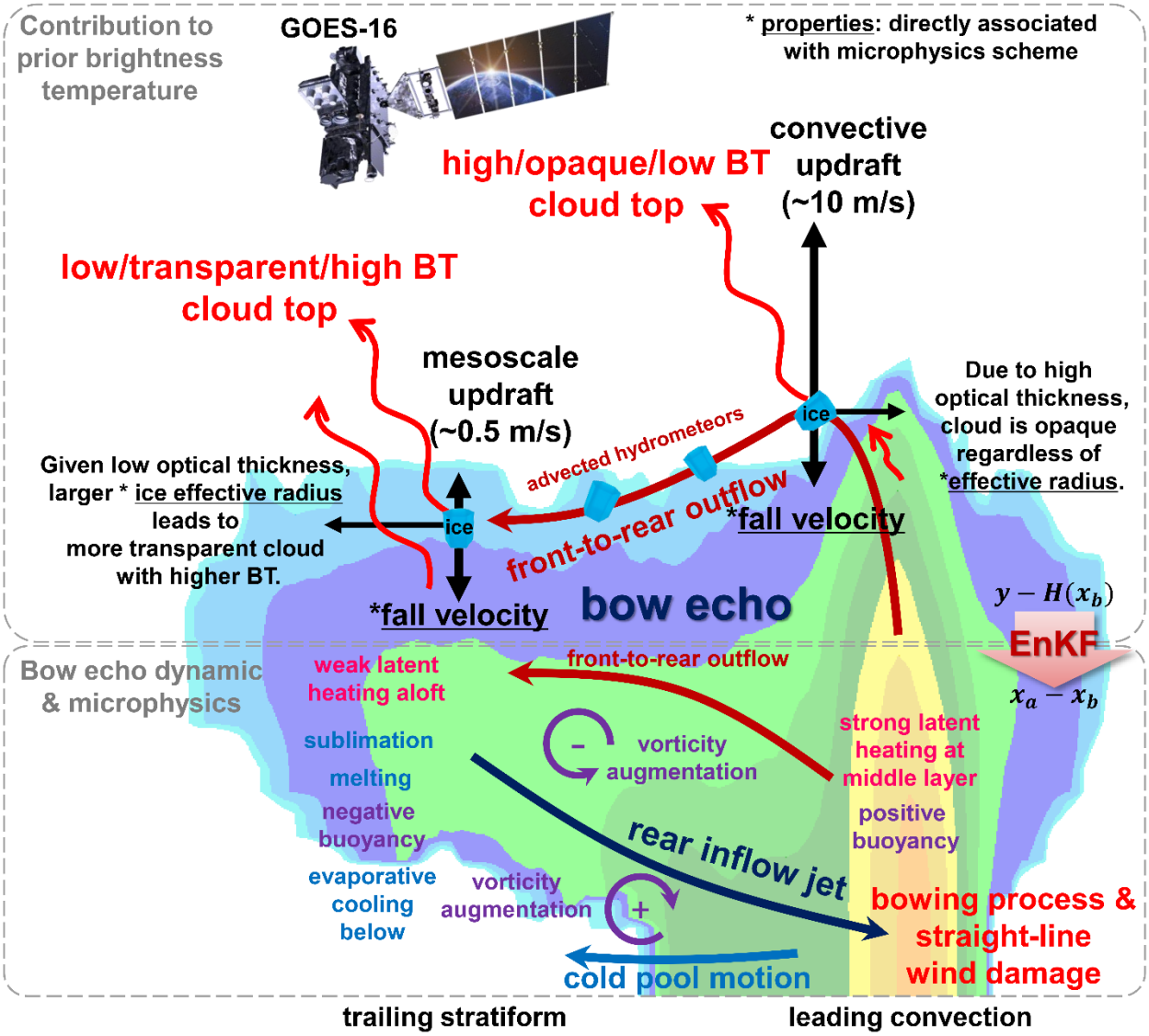

Fig. 16. Conceptual diagram of assimilating GOES-16 ABI infrared brightness temperatures with different microphysics parameterization schemes for a bow echo case.